SUPPORTING INFORMATION

Tailoring Porosity and Rotational Dynamics in a Series of Octacarboxylate Metal-Organic Frameworks

Florian Moreau,[a] Daniil I. Kolokolov,[b,h] Alexander G. Stepanov,[b,h] Timothy L. Easun,[c] Anne Dailly,[d] William Lewis,[e] Alexander J. Blake,[e] Harriott Nowell,[f] Matthew J. Lennox,[e] Elena Besley,[e] Sihai Yang,[a]* and Martin Schröder[a,g]*

[a] *School of Chemistry, University of Manchester, Oxford Road, Manchester M13 9PL, U.K.*

[b] *Boreskov Institute of Catalysis, Siberian Branch of Russian Academy of Sciences, Prospekt Akademika Lavrentieva 5, Novosibirsk 630090, Russia.*

[c] *School of Chemistry, Cardiff University, Main Building, Park Place, Cardiff CF10 3AT, U.K.*

[d] *General Motors Global Research and Development Center, Warren, MI, USA*

[e] *School of Chemistry, University of Nottingham, University Park, Nottingham NG7 2RD, U.K.*

[f] *Diamond Light Source, Harwell Science Campus, Oxon, OX11 0DE, UK.*

[g] *Nikolaev Institute of Inorganic Chemistry, Siberian Branch of the Russian Academy of Sciences, 3 Acad. Lavrentiev Ave., Novosibirsk, 630090, Russia.*

[h.] *Novosibirsk State University, Pirogova Street 2, Novosibirsk 630090, Russia.*

Experimental Section

All chemical reagents and gases were obtained from commercial sources and unless otherwised noted used without further purification. 2-(4-Bromophenyl)-2,3-dihydro-1H-naphtho[1,8-de][1,3,2]diazaborinine, 1,1,2,2-tetrakis(4-bromophenyl)ethane, 3,5-bis(ethoxycarbonyl)phenylboronic acid, 2,3,6,7-tetraiodonaphthalene and dibenzo[b,e][1,4]dioxine-2,3,7,8-tetraamine tetrahydrochloride salt were prepared according to previously published procedures.[1–5] ^{1}H and ^{13}C NMR were measured on Bruker DPX 300, Bruker AV400, or Bruker AV(III)500 spectrometers. Residual protonated species in the deuterated solvents were used as internal references. Mass spectrometry was performed on a Bruker MicroTOF with the sample dissolved in methanol or acetonitrile. MALDI was performed on a Bruker Ultraflex III spectrometer and analysed using Flex Analysis software. Elemental analyses were measured on a CE-440 Elemental Analyzer provided by Departmental Analytical Services at the Universities of Nottingham and Manchester.

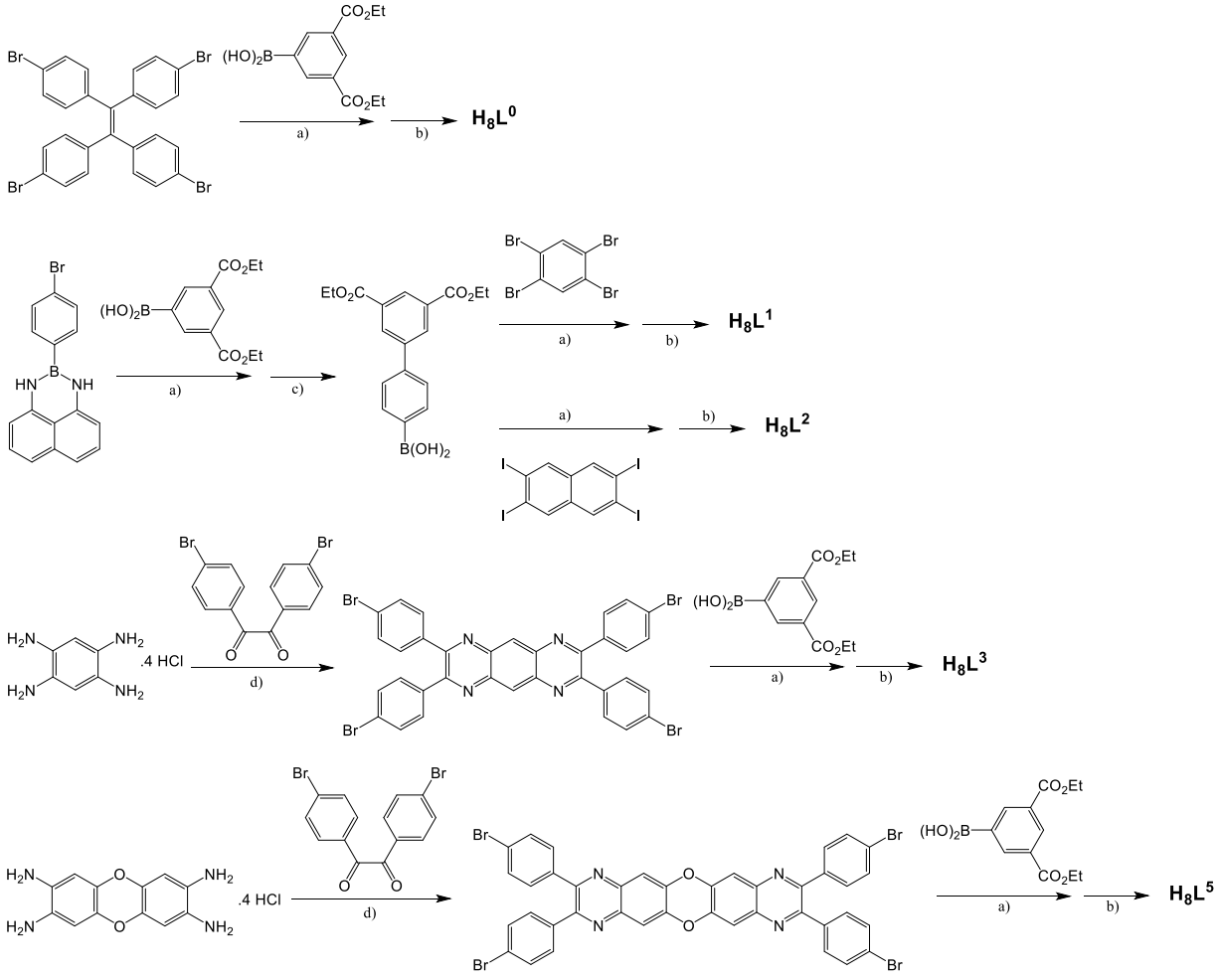

Scheme S1. Synthesis of linkers. Reagents and conditions: a) Pd_2dba_3, $P(^tBu)_3$, K_2CO_3, toluene/water, 80 °C, 1 h; b) NaOH, THF, EtOH, H_2O, 80 °C, 16 h; c) H_2SO_4, THF, H_2O, 80 °C, 16 h; d) 2-iodoxybenzoic acid, $MeCO_2H$, 120 °C, 16 h.

Preparation of 3',5'-bis(ethoxycarbonyl)biphenyl-4-ylboronic acid. 2-(4-Bromophenyl)-2,3-dihydro-1*H*-naphtho[1,8-*de*][1,3,2]diazaborinine (4.0 g, 12.4 mmol), 3,5-bis(ethoxycarbonyl)phenylboronic acid (3.8 g, 14.28 mmol) and K_2CO_3 (2.5 g, 18.1 mmol) were added to a mixture of toluene and deionized water (500 mL; 4:1 v/v). The resulting suspension was degassed under Ar for 20 min and heated at 60 °C. While stirring at 60 °C under Ar, tri-*tert*-butylphosphine (1M in toluene, 3.0 mL) and [$Pd_2(dba_3)$] (dba = dibenzylideneacetone) (1.0 g, 1.09 mmol) were added sequentially. After addition, the reaction was heated to 80 °C for 1 h. The resulting mixture was filtered while hot and once cooled to room temperature the filtrate was extracted with CH_2Cl_2 (3 × 150 mL). The combined extracts were dried over $MgSO_4$ and the solvent removed *in vacuo*. Recrystallization from CH_2Cl_2/hexane afforded diethyl 4'-(1*H*-naphtho[1,8-*de*][1,3,2]diazaborinin-2(3*H*)-yl)biphenyl-3,5-dicarboxylate as a yellow solid which was dissolved in THF (400 mL), aqueous H_2SO_4 (2M, 70 mL) was added and the solution refluxed for 16 h. The resulting suspension was filtered and the precipitate discarded. The filtrate was concentrated *in vacuo* to 100 mL and deionized H_2O added to the residue to precipitate the product. The white solid was isolated by filtration, thoroughly washed with deionized water, and dried. Yield: 3.1 g, 72 %. ^{1}H NMR: (300 MHz, DMSO-d_6) δ/ppm = 8.42 (t, *J* = 1.5 Hz, 1H, ArH), 8.38 (d, *J* = 1.6 Hz, 2H, ArH), 7.93 (d, *J* = 8.2 Hz, 2H, ArH), 7.69 (d, *J* = 8.2 Hz, 2H, ArH), 4.38 (q, *J* = 7.1 Hz, 4H, Et), 1.35 (t, *J* = 7.1 Hz, 6H, Me); ^{13}C NMR: (75 MHz, $CDCl_3$), δ/ppm = 166.9 (C), 140.9 (C), 140.7 (C), 139.2 (C), 137.3 (C), 132.6 (CH), 131.6 (CH), 131.0 (CH), 129.2 (C), 128.5 (CH), 127.3 (CH); MS: (ESI) Calcd: 343.134 Found: 343.135 (100 %) $[MH]^+$.

Preparation of 2,3,7,8-tetrakis(4-bromophenyl)pyrazino[2,3-*g*]quinoxaline. 1,2,4,5-Tetraaminobenzene tetrahydrochloride (0.5 g, 1.76 mmol), 4,4'-dibromobenzil (1.30 g, 3.52 mmol) and 2-iodoxybenzoic acid (45 wt%, 18.3 mg, 0.03 mmol) were dissolved in glacial acetic acid (70 mL). The resulting solution was heated to reflux for 16 h and then cooled. Upon addition of deionized H_2O the product precipitated as a yellow solid, which was isolated by filtration, washed with H_2O then EtOH, and dried in air. Yield: 1.158 g, 82 %; ^{1}H NMR: (400 MHz, CF_3CO_2D) δ/ppm = 9.70 (s, 2H, ArH), 7.90 (d, *J* = 8.8 Hz, 8H, ArH), 7.73 (d, *J* = 8.6 Hz, 8H, ArH); ^{13}C NMR: (100 MHz, CF_3CO_2D), δ/ppm = 156.8 (C), 136.5 (C), 132.9 (C), 131.4 (CH), 130.5 (CH), 129.8 (CH), 123.5 (C); MS: (APCI) Calcd: 802.829 Found: 802.828 $[MH]^+$.

Preparation of [1,4]Dioxino[2,3-*g*:5,6-*g*']diquinoxaline-2,3,9,10-tetra-4-bromophenyl. Dibenzo[b,e][1,4]dioxine-2,3,7,8-tetraamine tetrahydrochloride salt (860 mg, 2.20 mmol), 4,4'-dibromobenzil (1.62 g, 4.40 mmol) and 2-iodoxybenzoic acid (stabilized, 45 wt%, 54 mg, 0.09 mmol) were dissolved in glacial acetic acid (125 mL). The resulting solution was heated to reflux for 16 h then allowed to cool. Upon addition of deionized H_2O the product precipitated, was isolated by filtration, washed with water then EtOH, and dried to yield brown solid. Yield: 1.725 g, 86%. ^{1}H NMR: (400 MHz, CF_3CO_2D) δ/ppm = 8.23 (s, 4H, ArH), 7.76 (d, *J* = 8.5 Hz, 8H, ArH), 7.52 (d, *J* = 8.5 Hz, 8H, ArH); ^{13}C NMR: (125 MHz, CF_3CO_2D), δ/ppm = 151.2 (C), 146.3 (C), 135.5 (C), 132.8

(C), 130.9 (CH), 129.9 (CH), 128.4 (C), 109.2 (CH); MS (MALDI-TOF, dithranol matrix, positive mode) Calcd: 908.8 Found: 908.9 $[MH]^+$.

Preparation of ligands

The ligands H_8L^0, H_8L^1, H_8L^2, H_8L^3 and H_8L^5 (H_8L^0 = 4',4''',4'''',4'''''-(ethene-1,1,2,2-tetrayl)tetrakis(([1,1'-biphenyl]-3,5-dicarboxylic acid)), H_8L^1 = 4',4''',4'''',4'''''-(benzene-1,2,4,5-tetrayl)tetrakis(([1,1'-biphenyl]-3,5-dicarboxylic acid)), H_8L^2 = 4',4''',4'''',4'''''-(naphthalene-2,3,6,7-tetrayl)tetrakis(([1,1'-biphenyl]-3,5-dicarboxylic acid)), H_8L^3 = 4',4''',4'''',4'''''-(pyrazino[2,3-g]quinoxaline-2,3,7,8-tetrayl)tetrakis(([1,1'-biphenyl]-3,5-dicarboxylic acid)), H_8L^5 = 4',4''',4'''',4'''''-([1,4]dioxino [2,3-*g*:5,6-*g*']diquinoxaline-2,3,9,10-tetrayl)tetrakis(([1,1'-biphenyl]-3,5-dicarboxylic acid))) were all synthesized using a Suzuki-Miyaura coupling reaction between the corresponding tetrahalogenated core and boronic acid, followed by hydrolysis of the ester functions. The synthesis of H_8L^1 is described in detail.

Preparation of H_8L^1. 1,2,4,5-Tetrabromobenzene (0.3 g, 0.76 mmol), 3',5'-bis(ethoxycarbonyl)biphenyl-4-ylboronic acid (1.1 g, 3.21 mmol) and K_2CO_3 (0.45 g, 3.26 mmol) were added to a mixture of toluene and deionized H_2O (150 mL; 4:1 v/v) and the resulting suspension was degassed under Ar for 20 min and then heated to 60 °C. While stirring at 60 °C under Ar, P(*t*-Bu)$_3$ (1M in toluene, 0.5 mL) and then $[Pd_2(dba)_3]$ (0.18 g, 0.2 mmol) were added. The reaction mixture was heated to 80 °C for 1 h under Ar. The resultant mixture was filtered through a sintered funnel while hot and once cooled to room temperature the filtrate was extracted with CH_2Cl_2 (3 × 100 mL). The combined extracts were dried over $MgSO_4$, and the solvent removed *in vacuo*. The residue was re-dissolved in CH_2Cl_2 (50 mL) and the octa-ethyl ester of the target ligand was precipitated by addition of hot MeOH (100 mL) and isolated by filtration while hot (0.7 g, 73%) as an off white solid. The ester was dissolved in THF and EtOH (200 mL; 1:1 v/v), an aqueous solution of NaOH (2M, 100 mL) added, and the mixture refluxed for 16 h. The resultant solution was concentrated *in vacuo* to 100 mL and acidified to pH 2-3 using concentrated hydrochloric acid. The precipitate was isolated by filtration, thoroughly washed with water, and recrystallized from N,N'-dimethylformamide/H_2O to afford pure H_8L^1 as a white solid. Yield: 0.52 g, 90 %. ^{1}H NMR: (400 MHz, DMSO-d6), δ/ppm = 13.37 (sbr, 8H, COOH), 8.44 (s, 4H, ArH), 8.39 (s, 8H, ArH), 7.73 (d, J = 8.3 Hz, 8H, ArH), 7.63 (s, 2H, ArH), 7.48 (d, J = 8.3 Hz, 8H, ArH); ^{13}C NMR: (100 MHz, DMSO-d6), δ/ppm = 166.9 (C), 140.9 (C), 140.7 (C), 139.2 (C), 137.3 (C), 132.6 (CH), 131.6 (CH), 131.0 (CH), 129.2 (C), 128.5 (CH), 127.3 ppm (CH); MS (ESI) Calcd: 1037.209 Found: 1037.203 $[M-H]^-$.

H_8L^0. ^{1}H NMR: (400 MHz, DMSO-d6), δ/ppm = 13.27 (sbr, 8H, COOH), 8.41 (s, 4H, ArH), 8.34 (s, 8H, ArH), 7.63 (d, J = 8.1 Hz, 8H, ArH), 7.24 (d, J = 8.1 Hz, 8H, ArH); ^{13}C NMR: (100 MHz, DMSO-d6), δ/ppm = 167.0 (C), 143.5 (C), 141.9 (C), 140.7 (C), 137.0 (C), 132.6 (C), 132.5 (CH), 131.5 (CH), 129.3 (CH), 126.9 ppm (CH); MS (ESI) Calcd: 987.293 Found 987.282 $[M-H]^-$

H_8L^2. ^{1}H NMR: (400 MHz, DMSO-d6), δ/ppm = 13.35 (sbr, 8H, COOH), 8.43 (s, 4H, ArH), 8.37 (s, 8H, ArH), 7.71 (d, J = 8.3 Hz, 8H, ArH), 7.58 (s, 4H, ArH), 7.44 (d, J = 8.3 Hz, 8H, ArH); ^{13}C NMR:

(100 MHz, DMSO-d6), δ/ppm = 166.9 (C), 141.3 (C), 140.8 (C), 138.7 (C), 137.1 (C), 132.5 (C), 131.6 (CH), 131.0 (CH), 130,1(CH), 129.3 (CH), 128.1 (C), 127.1 ppm (CH); MS (ESI) Calcd: 1087.223 Found 1087.227 $[M-H]^-$

H_8L^3. ^{1}H NMR: (400 MHz, DMSO-d6), δ/ppm = 13.39 (sbr, 8H, COOH), 8.89 (s, 2H, ArH), 8.44 (s, 4H, ArH), 8.39 (s, 8H, ArH), 7.80 (d, J = 8.2 Hz, 8H, ArH), 7.76 (d, J = 8.2 Hz, 8H, ArH); ^{13}C NMR: (100 MHz, DMSO-d6), δ/ppm = 166.8 (C), 154.8 (C), 140.5 (C), 140.2 (C), 139.6 (C), 138.6 (C), 132.5 (CH), 131.7 (CH), 131.3 (CH), 129.6 (CH), 128.4 (CH), 127.1 ppm (CH); MS (APCI) Calcd: 1143.236 Found: 1143.238 $[MH]^+$)

H_8L^5. ^{1}H NMR: (400 MHz, CF_3CO_2D), δ/ppm = 9.05 (s, 4H, ArH), 8.82 (s, 8H, ArH), 8.33 (s, 4H, ArH), 8.01 (d, J = 7.2 Hz, 8H, ArH), 7.94 (d, J = 7.4 Hz, 8H, ArH); ^{13}C NMR: (125 MHz, CF_3CO_2D), δ/ppm = 171.2 (C), 151.6 (C), 146.4 (C), 143.0 (C), 140.9 (C), 135.7 (C), 134.0 (CH), 131.7 (C), 130.8 (CH), 130.2 (CH), 129.9 (CH), 128.0 (C), 109.1 ppm (CH); MS (APCI) Calcd: 1249.241 Found: 1249.240 [MH]+)

Preparation of selectively deuterated linkers

The deuterated linkers were synthesised following the same procedures as above but starting from deuterated building blocks: 1,1,2,2-tetrakis(4-bromophenyl)ethane-d_{16} and 2,3-dihydro-1H-naphtho[1,8-de][1,3,2]diazaborinine-d_4 which were synthesised as previously reported.[1,6]

d_{16}-H_8L^0. ^{1}H NMR: (400 MHz, DMSO-d_6), δ/ppm = 13.35 (sbr, 8H, COOH), 8.42 (s, 4H, ArH), 8.33 (s, 8H, ArH); ^{13}C NMR: (100 MHz, DMSO-d_6), δ/ppm = 166.9 (C), 143.3 (C), 140.5 (C), 140.6 (C), 136.7 (C), 132.5 (C), 131.7 (CD), 131.4 (CH), 129.2 (CH), 126.4 ppm (CD); MS(ESI) Calcd: 1003.294 Found: 1003.287 (100 %) $[M-H]^-$.

d_{16}-H_8L^1. ^{1}H NMR: (400 MHz, DMSO-d_6), δ/ppm = 13.36 (sbr, 8H, COOH), 8.43 (s, 4H, ArH), 8.37 (s, 8H, ArH), 7.61 (s, 2H, ArH); ^{13}C NMR: (100 MHz, DMSO-d_6), δ/ppm = 166.9 (C), 140.8 (C), 140.5 (C), 139.1 (C), 137.1 (C), 133.4 (CH), 132.5 (C), 131.6 (CH), 130.53 (CD), 129.3 (CH), 126.8 ppm (CD); MS (ESI) Calcd: 1053.3091 Found: 1053.3028 (100 %) $[M-H]^-$.

Preparation of MOF materials

Yields were calculated based on TGA of the as-synthesized materials since the precise solvent content within the pores is variable, rendering evaluation by means of elemental analysis can thus be problematic. Therefore, elemental analyses of materials were performed after activation of the materials and re-hydration upon exposure under standard conditions so that the exact water content of the framework could be evaluated by TGA.

Preparation of MFM-180:

H_8L^0 (0.30 g, 0.30 mmol) and $CuCl_2$ (0.19 g, 1.40 mmol) were dissolved in N,N'-diethylformamide (30 mL). EtOH (30 mL) and an aqueous solution of HCl (0.1M, 15 mL) were added to the resulting solution, which was placed in a tightly capped 250 mL Duran® pressure plus laboratory bottle (cat. n° 1092234). The solution was heated at 80 °C in an oven for 16 h, and a large amount of crystalline

product precipitated. The blue crystal plates were isolated by filtration while the mother liquor was still warm and washed sequentially with warm DMF and MeOH and then dried in air (yield: 0.52 g, 79 %). After activation and rehydration, $[Cu_4(L^0)(H_2O)_4]\cdot 7H_2O$ was obtained; elemental analysis: Calcd: C, 48.61; H, 3.52; Found: C, 48.93; H, 3.20 %.

Preparation of MFM-181:

H_8L^1 (0.31 g, 0.30 mmol) and $CuCl_2$ (0.19 g, 1.40 mmol) were dissolved in N,N'-diethylformamide (30 mL). EtOH (30 mL) and an aqueous solution of HCl (0.1M, 15 mL) were added to the resulting solution, which was placed in a tightly capped 250 mL Duran® pressure plus laboratory bottle. The solution was heated at 80 °C in an oven for 16 h, and a large amount of crystalline product precipitated. The large blue plate-shaped crystals were isolated by filtration while the mother solution was still warm and washed sequentially with warm DMF and MeOH, then dried in air (yield: 0.48 g, 68 %). After activation and rehydration, $[Cu_4(L^1)(H_2O)_4]\cdot 11H_2O$ was obtained; elemental analysis: Calcd: C, 47.88; H, 3.89; Found: C, 47.95; H, 3.90 %.

Preparation of MFM-182: H_8L^2 (0.010 g, 0.009 mmol) and $CuCl_2$ (0.006 g, 0.045 mmol) were dissolved in N,N'-diethylformamide (1 mL). EtOH (1 mL) and an aqueous solution of HCl (0.1M, 0.5 mL) were added to the resulting solution, which was placed in a tightly capped 8 mL Pyrex vial. The solution was heated at 80 °C in an oven for 16 h, and blue plate-shaped crystals precipitated.

Preparation of MFM-183:

H_8L^3 (0.34 g, 0.30 mmol) and $CuCl_2$ (0.19 g, 1.40 mmol) were dissolved in N,N'-diethylformamide (30 mL). EtOH (30 mL) and an aqueous solution of HCl (0.1M, 15 mL) were added to the resulting solution, which was placed in a tightly capped 250 mL Duran® pressure plus laboratory bottle. The solution was heated at 80 °C in an oven for 16 h, and a large amount of crystalline product precipitated. The large green plate-shaped crystals were isolated by filtration while the mother solution was still warm and washed sequentially with warm DMF and MeOH, then dried in air (yield: 0.56 g, 75 %). After activation and rehydration, $[Cu_4(L^3)H_2O)_4]\cdot 12H_2O$ was obtained; elemental analysis: Calcd: C, 47.26; H, 3.73; N, 3.34; Found: C, 48.75; H, 3.33; N, 3.49 %.

Preparation of MFM-185:

H_8L^5 (0.125 g, 0.10 mmol) and $Cu(NO_3)_2\cdot 2.5H_20$ (0.50 g, 2,15 mmol) were dissolved in DMSO (25 mL). *N*,*N'*-Dimethylformamide (50 mL) and an aqueous solution of HCl (2M, 1.25 mL) were added to the resulting solution, which was placed in a tightly capped 250 mL Duran® pressure plus laboratory bottle. The solution was heated at 80°C in an oven for 5 days, and a large amount of crystalline product precipitated. The green plate-shaped crystals were isolated by filtration while the mother solution was still warm and washed sequentially with hot DMSO and MeOH, then dried in air (yield: 0.45 g, 71 %). After activation and rehydration, $[Cu_4(L^5)(H_2O)_4]\cdot 10H_2O$ was obtained; elemental analysis: Calcd: C, 49.49; H, 3.46; N, 3.09; Found: C, 48.65; H, 3.01; N, 3.23 %.

Preparation of selectively deuterated MOFs

The deuterated MOFs were synthesised following the same procedures starting from deuterated linkers

X-ray Crystallography

Single crystal X-ray diffraction structure determinations

Single crystal diffraction datasets for MFM-180, MFM-181 and MFM-182 were collected at 120 K using an Agilent GV1000 diffractometer, and for MFM-183 and MFM-185 using synchrotron radiation on Beamline I19 at Diamond Light Source. Details of data collection and processing procedures are included in the CIF files. Structures were solved by direct methods using SHELXS[7] and remaining atoms were localised from successive difference Fourier maps using SHELXL.[8] The hydrogen atoms from the linkers and the coordinating water molecules were placed geometrically and refined using a riding model. The refinement of the framework was performed by ignoring the contribution of the disordered solvent molecules. The region containing the disordered electron density was identified by considering the van der Waals radii of the atoms constituting the ordered framework. The contribution of this region to the total structure factor was calculated via a discrete Fourier transformation and subtracted in order to generate a new set of *hkl* reflections by means of the program SQUEEZE.[9]

Table S1. Crystal data and structure refinement details for MFM-180

Identification code	MFM-180
Chemical formula	$(C_{58}H_{36}Cu_4O_{20})$
M_r (g mol^{-1})	2178.21
Crystal system, space group	Tetragonal, $I\bar{4}2m$
Temperature (K)	120
a, c (Å)	18.69242 (16), 35.9196 (4)
V (Å^3)	12550.6 (2)
Z	4
Radiation type	Cu $K\alpha$
μ (mm^{-1})	1.38
Crystal size (mm)	0.09 × 0.07 × 0.03
Absorption correction	Gaussian .
T_{min}, T_{max}	0.911, 0.965
No. of measured, independent and observed [$I > 2s(I)$] reflections	36516, 6651, 6228
R_{int}	0.035
(sin θ/ λ)max (Å-1)	0.626
$R[F^2 > 2s(F^2)]$, $wR(F^2)$, S	0.029, 0.083, 1.04
No. of reflections	6651
No. of parameters	195
H-atom treatment	H-atom parameters constrained
$D\rho_{max}$, $D\rho_{min}$ (e Å^{-3})	0.48, -0.20
Absolute structure	Refined as an inversion twin.
Absolute structure parameter	0.64 (3)

Table S2. Crystal data and structure refinement details for MFM-181

Identification code	MFM-181
Chemical formula	$(C_{62}H_{38}Cu_4O_{20})$
M_r	2556.59
Crystal system, space group	Tetragonal, $I4/mmm$
Temperature (K)	120
a, c (Å)	18.5871 (5), 41.033 (2)
V (Å^3)	14176.0 (9)
Z	4
Radiation type	Cu $K\alpha$
μ (mm^{-1})	0.62
Crystal size (mm)	0.20 × 0.20 × 0.02
Absorption correction	Gaussian
T_{min}, T_{max}	0.890, 0.991
No. of measured, independent and observed [$I > 2s(I)$] reflections	29384, 4030, 2982
R_{int}	0.081
$(\sin \theta/\lambda)_{max}$ (Å^{-1})	0.625
$R[F^2 > 2s(F^2)]$, $wR(F^2)$, S	0.056, 0.174, 1.07
No. of reflections	4030
No. of parameters	129
No. of restraints	2
H-atom treatment	H-atom parameters constrained
$D\rho_{max}$, $D\rho_{min}$ (e Å^{-3})	0.94, -0.69

Table S3. Crystal data and structure refinement details for MFM-182

Identification code	MFM-182
Chemical formula	($C_{66}H_{40}Cu_4O_{20}$)
M_r	1407.14
Crystal system, space group	Tetragonal, *I*4/*mmm*
Temperature (K)	120
a, *c* (Å)	18.5802 (4), 45.903 (3)
V (Å^3)	15847 (1)
Z	4
Radiation type	Cu *K*α
μ (mm^{-1})	0.85
Crystal size (mm)	0.19 × 0.18 × 0.02
Absorption correction	Gaussian
T_{min}, T_{max}	0.876, 0.981
No. of measured, independent and observed [$I > 2s(I)$] reflections	20867, 4459, 2938
R_{int}	0.055
$(\sin \theta/\lambda)_{max}$ (Å^{-1})	0.625
$R[F^2 > 2s(F^2)]$, $wR(F^2)$, S	0.062, 0.205, 1.02
No. of reflections	4459
No. of parameters	135
No. of restraints	2
H-atom treatment	H-atom parameters constrained
$D\rho_{max}$, $D\rho_{min}$ (e Å^{-3})	0.35, −0.30

Table S4. Crystal data and structure refinement details for MFM-183

Identification code	MFM-183
Chemical formula	($C_{66}H_{38}Cu_4N_4O_{20}$)
M_r	3306.41
Crystal system, space group	Tetragonal, *I*4/*mmm*
Temperature (K)	120
a, *c* (Å)	18.6881 (3), 50.6437 (17)
V (Å^3)	17687.1 (7)
Z	4
Radiation type	Synchrotron, λ = 0.6889 Å
μ (mm^{-1})	0.52
Crystal size (mm)	0.2 × 0.2 × 0.02
Absorption correction	Multi-scan
T_{min}, T_{max}	0.774, 1.000
No. of measured, independent and observed [$I > 2s(I)$] reflections	115753, 8670, 4371
R_{int}	0.088
(sin θ/ λ)max (Å-1)	0.762
$R[F^2 > 2s(F^2)]$, $wR(F^2)$, S	0.083, 0.307, 1.09
No. of reflections	8670
No. of parameters	141
H-atom treatment	H-atom parameters constrained
$D\rho_{max}$, $D\rho_{min}$ (e Å^{-3})	0.51, -0.38

Table S5. Crystal data and structure refinement details for MFM-185

Identification code	MFM-185
Chemical formula	($C_{72}H_{40}Cu_4N_4O_{22}$)
M_r	3250.62
Crystal system, space group	Tetragonal, *I*4/*mmm*
Temperature (K)	293
a, *c* (Å)	18.476 (2), 59.999 (8)
V (Å^3)	20480 (4)
Z	4
Radiation type	Synchrotron, λ = 0.6889 Å
m (mm^{-1})	0.44
Crystal size (mm)	0.1 × 0.1 × 0.01
Absorption correction	Multi-scan
T_{min}, T_{max}	0.513, 1.000
No. of measured, independent and observed [I > 2s(I)] reflections	33932, 5441, 1852
R_{int}	0.132
(sin θ/ λ)$_{max}$ (Å^{-1})	0.610
$R[F^2 > 2s(F^2)]$, $wR(F^2)$, S	0.103, 0.400, 1.01
No. of reflections	5441
No. of parameters	153
H-atom treatment	H-atom parameters constrained
Dρ$_{max}$, Dρ$_{min}$ (e Å^{-3})	0.38, -0.43

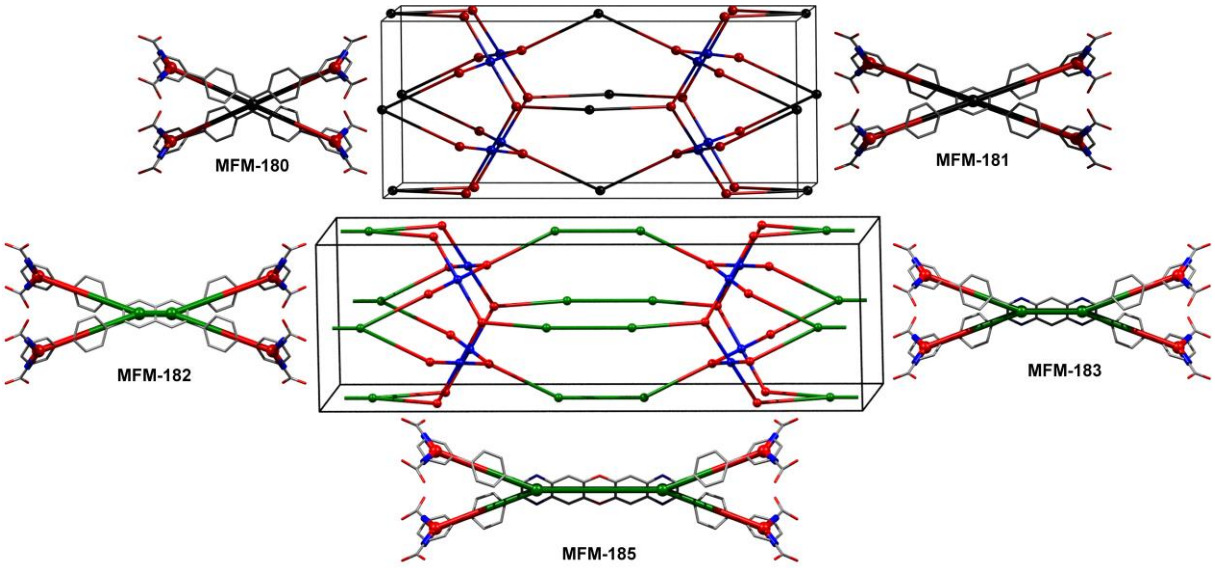

Figure S1. Topological simplification of the organic linkers and resulting **tbo** (top) and **3,3,4-c** (bottom) nets.

Powder X-ray diffraction (PXRD)

The phase purity of the bulk samples was confirmed by powder X-ray diffraction (Figure S4). Samples were activated, placed in a glovebox under Ar and then loaded into sample holders sealed with a polyimide (Kapton®) film. The PXRD measurements were carried out at room temperature on a PANalytical X'Pert PRO diffractometer using Cu-Kα radiation (λ = 1.5418 Å) at a scan speed of 0.02 °/s and a step size of 0.02 ° in 2θ. Desolvated frameworks MFM-180a and MFM-181a retain crystallinity upon exposure to air and humidity, whereas MFM-182a, MFM-183a and MFM-185a tend to collapse under ambient conditions.

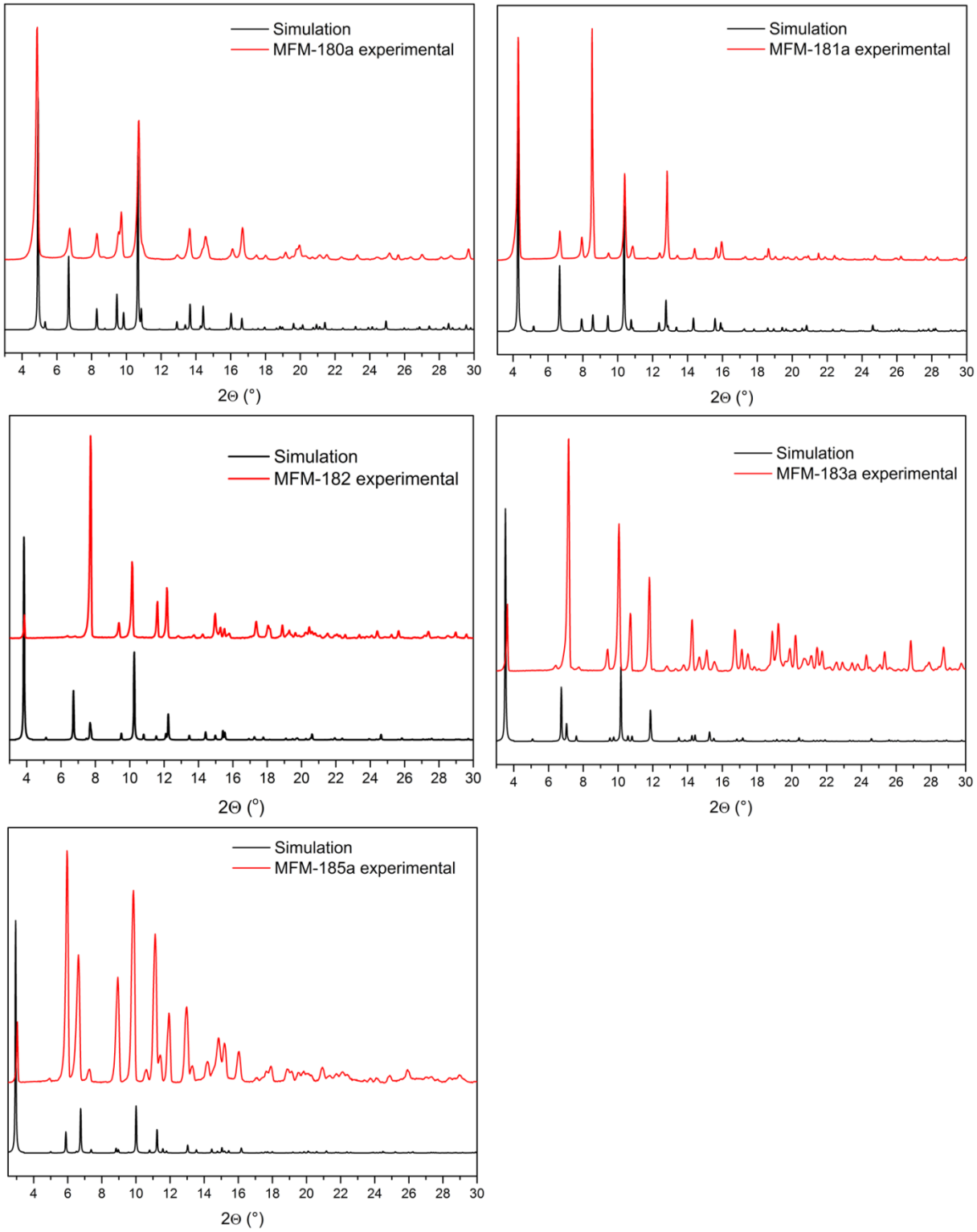

Figure S2. Experimental and simulated (from single crystal structures) PXRD patterns of MFM-180a, MFM-181a, MFM-182a, MFM-183a, and MFM-185a. The experimental patterns were collected under inert atmosphere using desolvated samples.

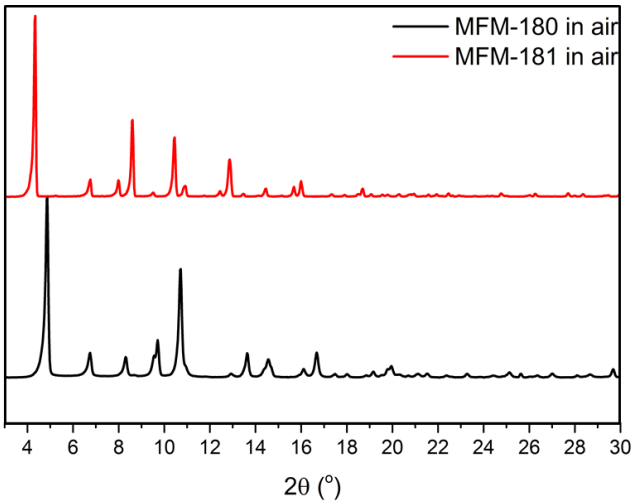

Figure S3. PXRD patterns of MFM-180 and MFM-181 after exposure of activated MFM-180a and MFM-181a to air for 24 hours.

Thermogravimetric analysis

The as-synthesized frameworks MFM-180, -181, -183 and -185 show very similar thermal behaviour and stability, as determined by thermogravimetric analysis (Figure S3). An initial rapid mass loss is observed between room temperature and 90 °C corresponding to the loss of uncoordinated EtOH and H_2O molecules from the pores, followed by a more gradual evacuation of bound H_2O molecules and solvents (DEF, DMF and/or DMSO) with higher boiling points. The material is stable between 180 °C and 300 °C without weight loss, followed by the rapid decomposition of the organic linker at higher temperatures.

TGA was performed under a flow of air with a heating rate of 5 °C/min using a Perkin Elmer Pyris 1 thermogravimetric analyser.

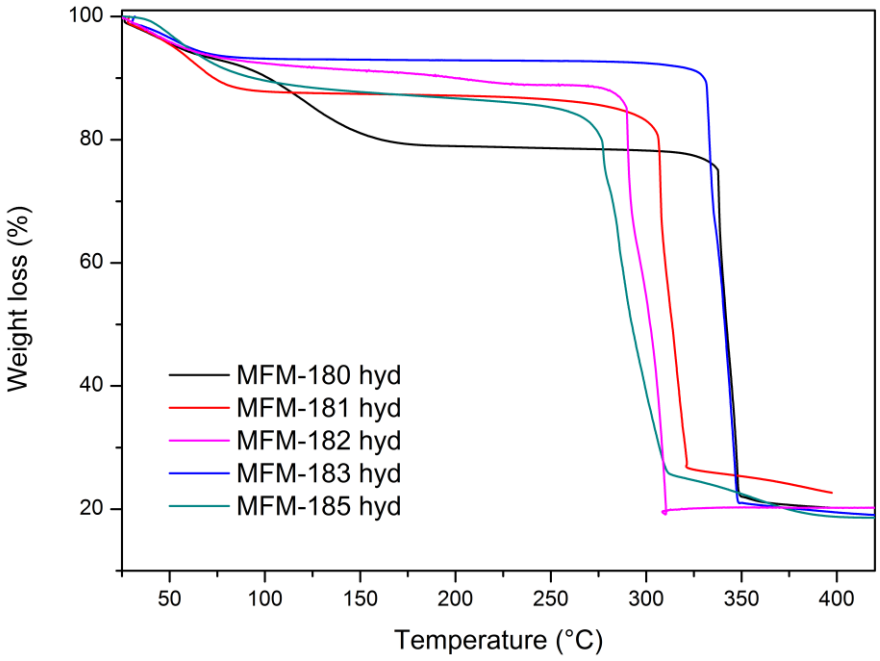

Figure S3. TGA plots of MFM-180, MFM-181, MFM-182, MFM-183 and MFM-185 after desolvation and exposure to ambient conditions.

Framework activation procedures

As-synthesised materials were solvent-exchanged with MeOH for 7 days. In the case of MFM-180 and MFM-181, the samples were then heated at 100 °C under dynamic vacuum for 16 h. In the case of MFM-183 and MFM-185, the MeOH exchanged samples were first activated *via* supercritical CO_2 drying using a Toumisis Autosamdri®-815, Series A critical point dryer, then transferred to a glovebox under Ar. The $ScCO_2$ dried samples were then transferred onto the gas adsorption instruments under inert atmosphere and heated at 100 °C under dynamic vacuum for 16 h.

N_2, H_2, CO_2 and CH_4 isotherms

Volumetric N_2, CO_2 and CH_4 isotherms for pressures in the range 0-1 bar were determined using a Quantachrome Instruments Autosorb-1. The data obtained was used for surface area and pore size distribution determination and for heat of adsorption calculations. For pressures in the range 0-20 bar, the H_2, CO_2 and CH_4 isotherms were measured on a Hiden Isochema intelligent gravimetric analyser (IGA). All data were corrected for the buoyancy of the system, samples and absorbates. Volumetric CH_4 sorption measurements were performed at General Motors over a pressure range of 0-60 bar using a HPVA-100 high-pressure analyzer (VTI Corporation). Sample tubes of a known weight were loaded with approximately 300 mg of sample under an argon atmosphere. All measurements were made with 99.9 % purity CH4, and 99.999 % purity He, the latter being used for dead volume measurements.

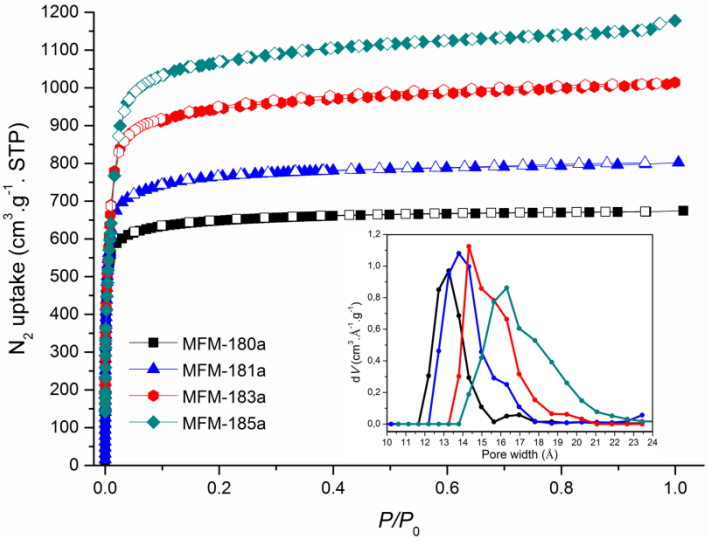

Figure S4. N_2 sorption isotherms for MFM-180a, -181a, -183a and -185a at 77 K. Insert shows pore size distributions. The pore size distributions of the materials were determined by analysis of the N_2 isotherms using a non-local density functional theory implementing a hybrid kernel based on a zeolite/silica model containing cylindrical pores as implemented in the Autosorb1 software package.

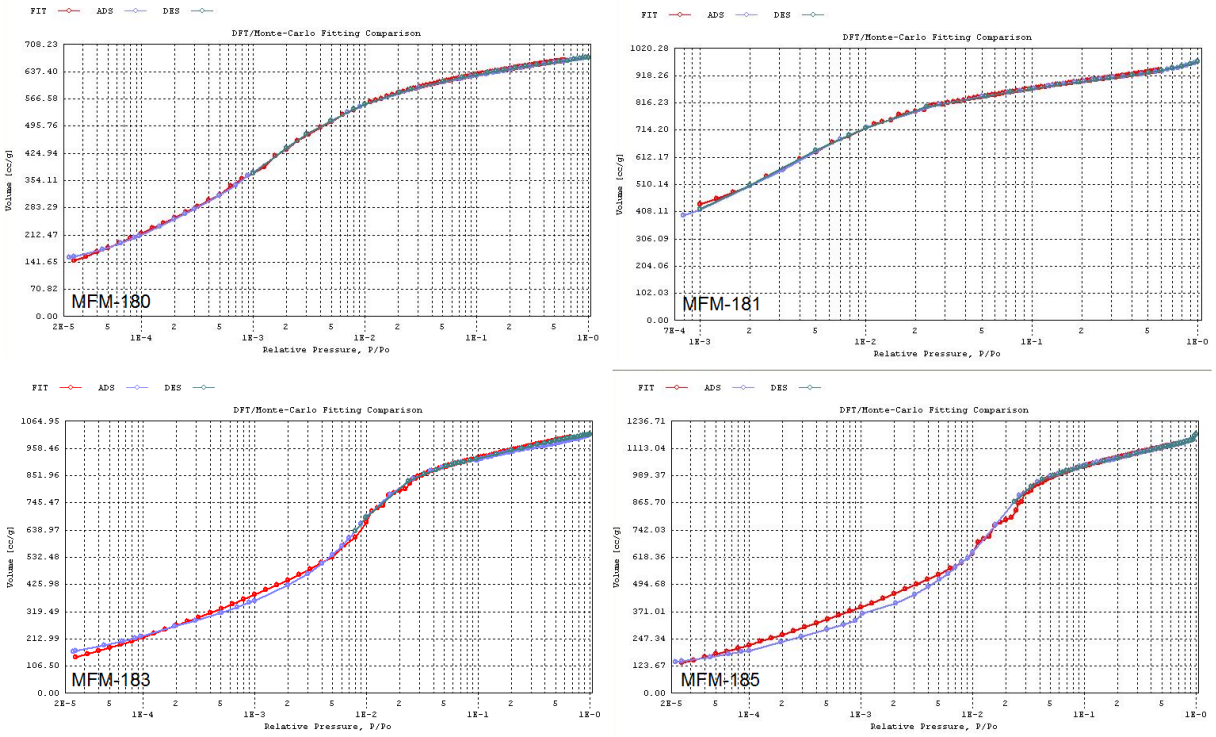

Figure S5. Comparison of NLDFT fitted and experimental N_2, 77K isotherms.

BET plots calculated from N_2 adsorption isotherms at 77K

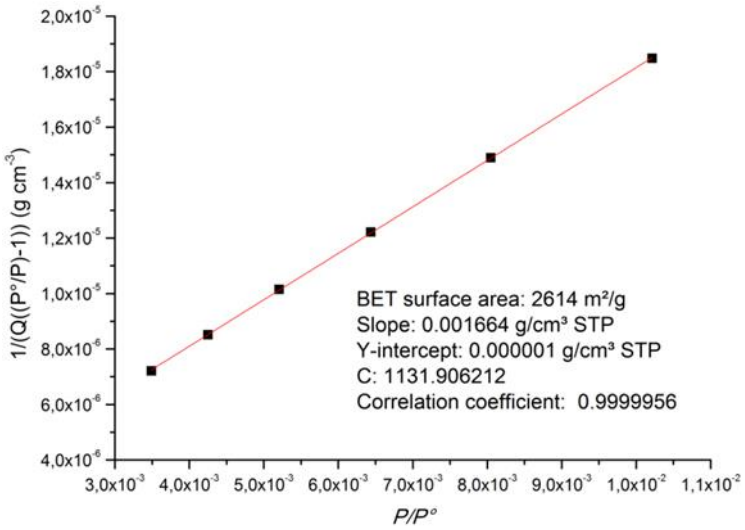

Figure S6. The BET plot derived from N_2 uptake in MFM-180a.

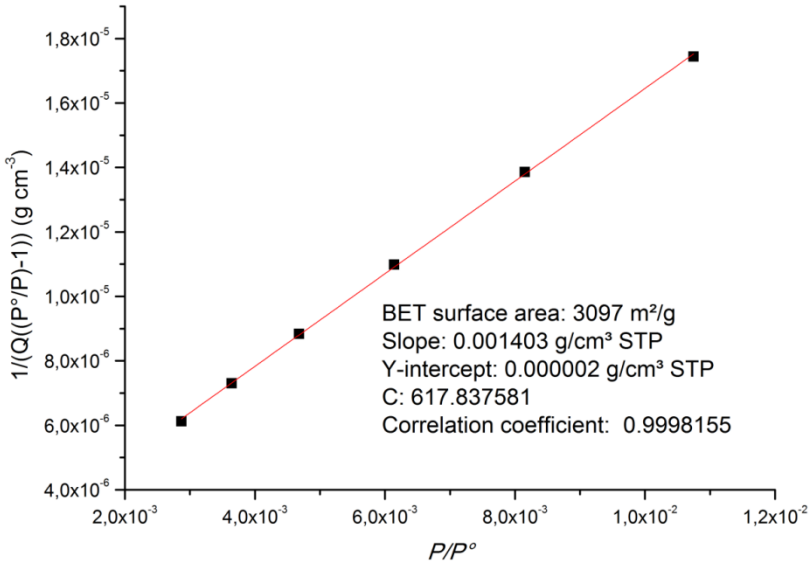

Figure S7. The BET plot derived from N_2 uptake in MFM-181a.

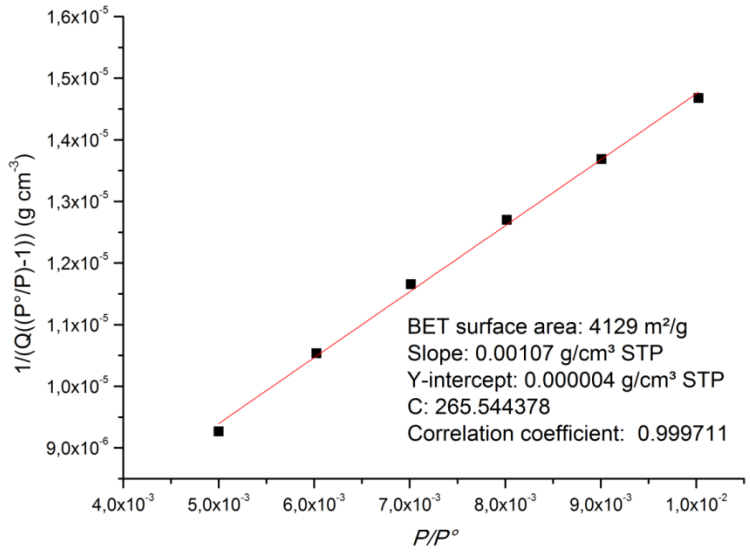

Figure S8. The BET plot derived from N_2 uptake in MFM-183a.

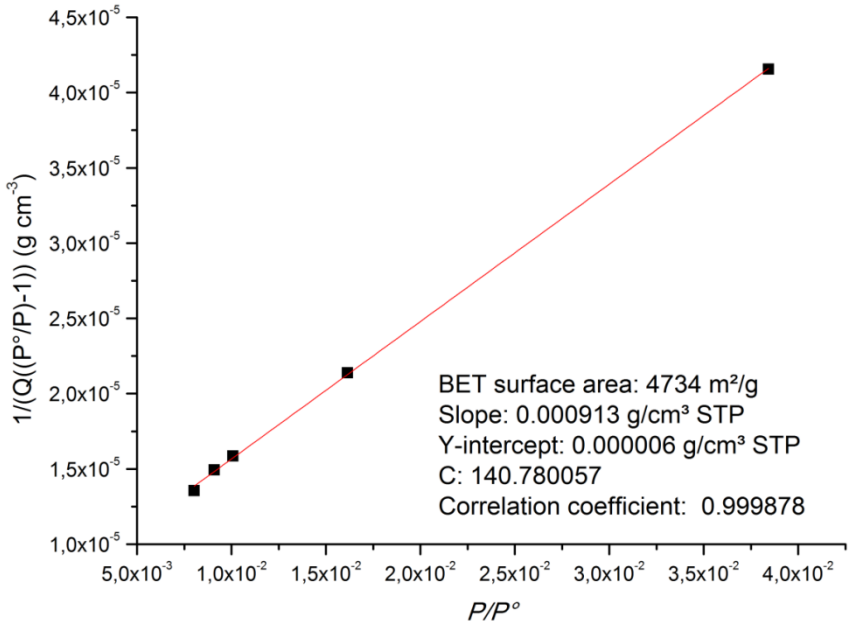

Figure S9. The BET plot derived from N_2 uptake in MFM-185a.

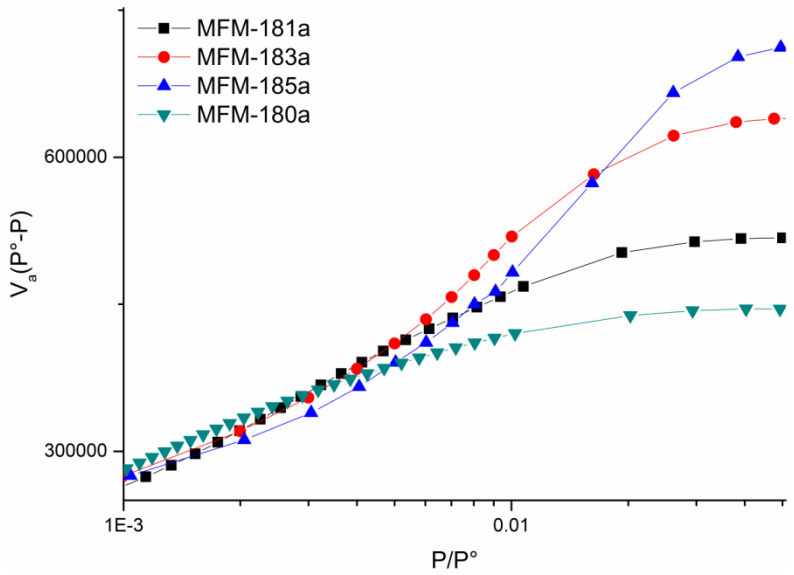

Figure S10. Consistency criterion[10] used to choose the P/P° range for the BET plots: Va(P° - P) plotted against P/P° for N_2, 77 K adsorption for framework materials.

***In Silico* Generation of MFM-184**

In lieu of successful synthesis of the H_8L^4 ligand targeted experimentally, the gas sorption properties of MFM-184 were calculated for a predicted crystal structure based on the assumption that the MOF is isoreticular to the other members of the MFM-18X series (Figure 3). The unit cell for MFM-184 was generated by first replacing the 5-fused heteroacene core of MFM-185 with a shorter, 4-fused core (Scheme 1) and reducing the length of the crystallographic *c*-axis to ensure appropriate connectivity within the structure. The cell parameters (a = b = 18.4760 Å, c = 55.2550 Å) and atomic coordinates were then optimised using the Forcite module implemented in Materials Studio, using the Universal Force Field[11] and charges calculated via the Electronegativity Equalization method.

BET plots calculated from simulated N_2 adsorption isotherms at 77K

The adsorption of N_2 at 77 K was simulated using the grand canonical Monte Carlo simulations implemented in the MuSiC software package[12] and using translation, rotation and energy-biased insertion and deletion moves. All simulations were allowed at least 8 x 106 equilibration steps, followed by 12 x 106 production steps for each pressure point. The frameworks were treated as rigid, with atoms kept fixed at their crystallographic positions. Lennard-Jones parameters for the framework atoms were taken from the OPLS[12] force field with the exception of copper, which is not included in the OPLS force field and for which UFF parameters[14] were used instead. Nitrogen was simulated as a rigid molecule using the TraPPE model,[15] incorporating both Lennard-Jones parameters and partial charges. Previous work has shown that nitrogen-MOF electrostatic contributions play only a minor

role in nitrogen adsorption[16] and, as such, only the electrostatic interactions between nitrogen molecules were included in our simulations.

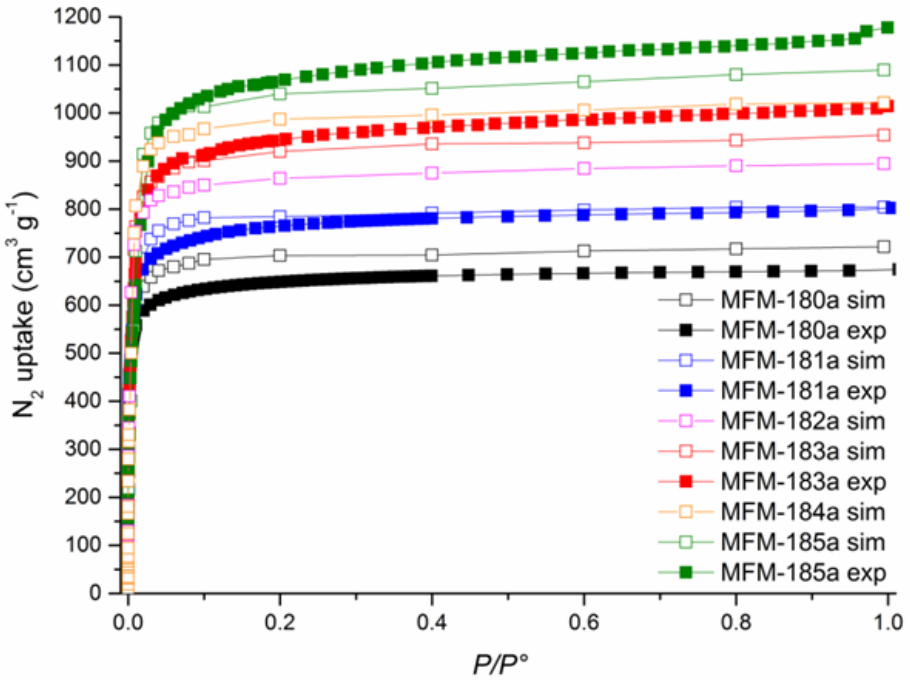

Figure S11. Simulated and experimental N_2 sorption isotherms for MFM-180a, -181a, -182a -183a, -184a and -185a at 77 K.

Based on the single crystal data at 100 K, the simulations are more than acceptable, and predict both the surface area (*i.e.*, the behaviour in the low to mid-loading regime) and the maximum uptake (*i.e.*, the accessible pore volume) of these MOFs to within 1-9% of experiment. A number of factors may account for any observed discrepancies: (i) a very small amount of solvent molecules may be retained within the pore structure of the desolvated MOFs; (ii) once desolvated, the MOFs may show slight distortion with possible change in pore geometry or volume. Thus, the low temperature single crystal data may not represent fully the powder crystalline samples, notwithstanding that PXRD data confirm the purity of bulk materials. The simulations can also be used as a methodology to evaluate the efficacy of activation of these materials.

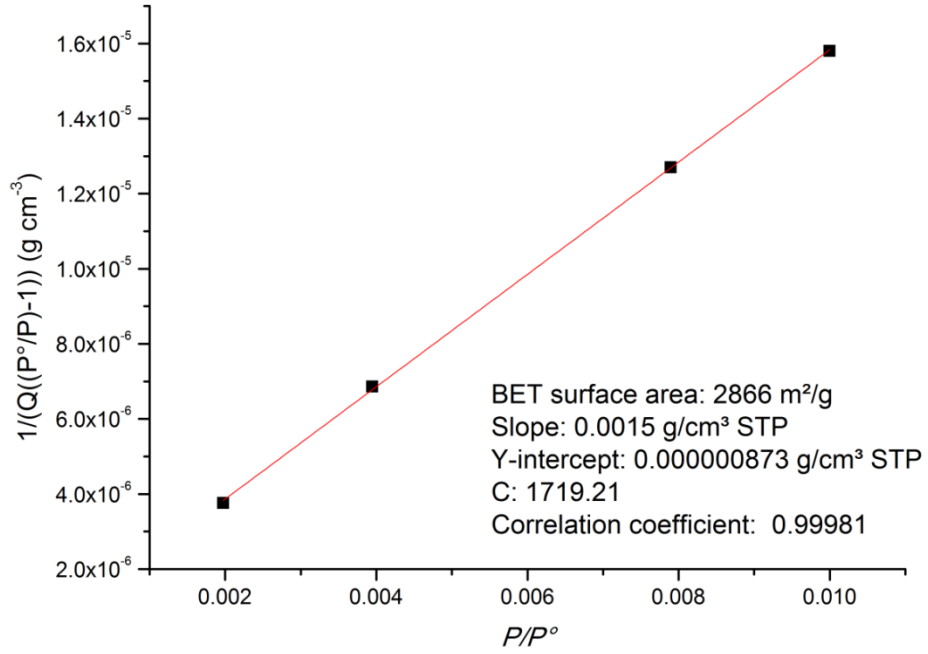

Figure S12. The BET plot derived from simulated N_2 uptake in MFM-180a.

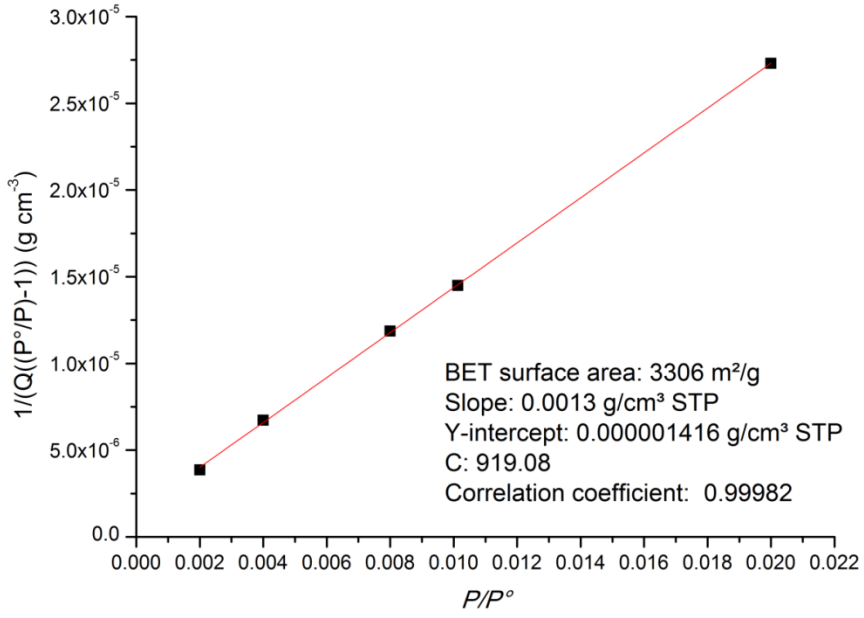

Figure S13. The BET plot derived from simulated N_2 uptake in MFM-181a.

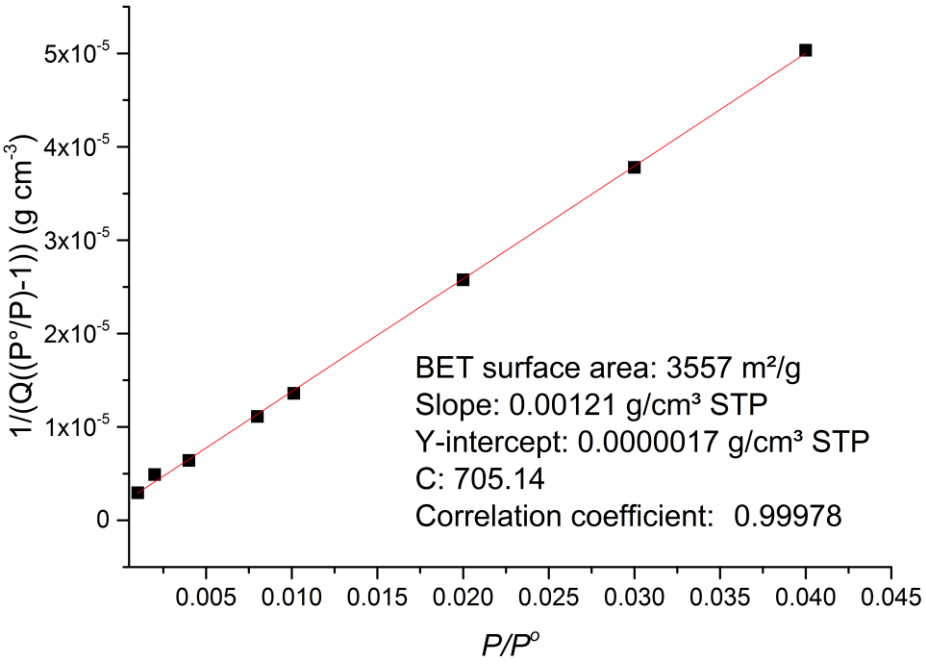

Figure S14. The BET plot derived from simulated N_2 uptake in MFM-182a.

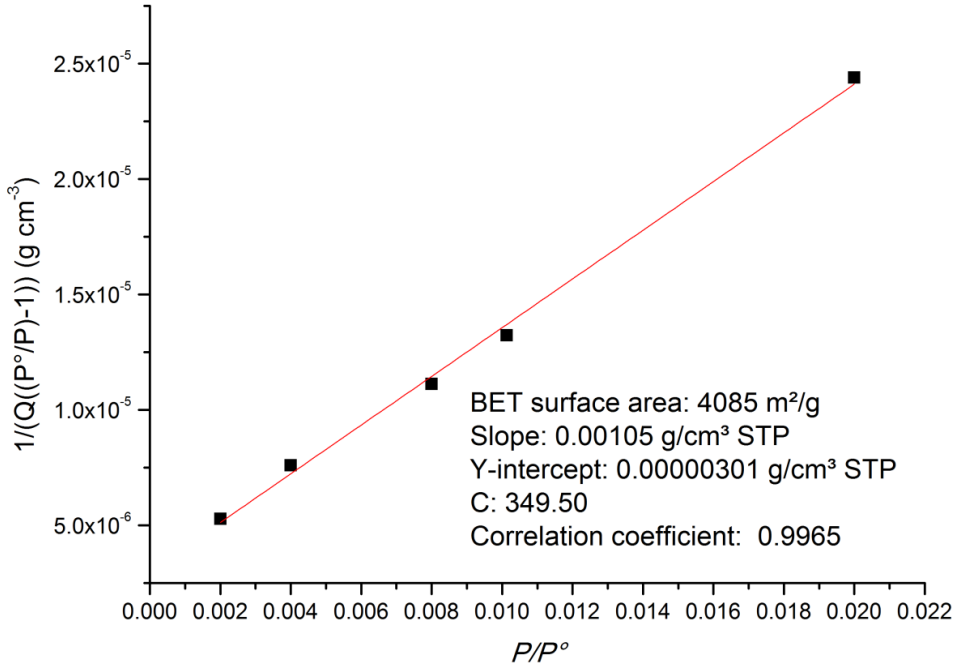

Figure S15. The BET plot derived from simulated N_2 uptake in MFM-183a.

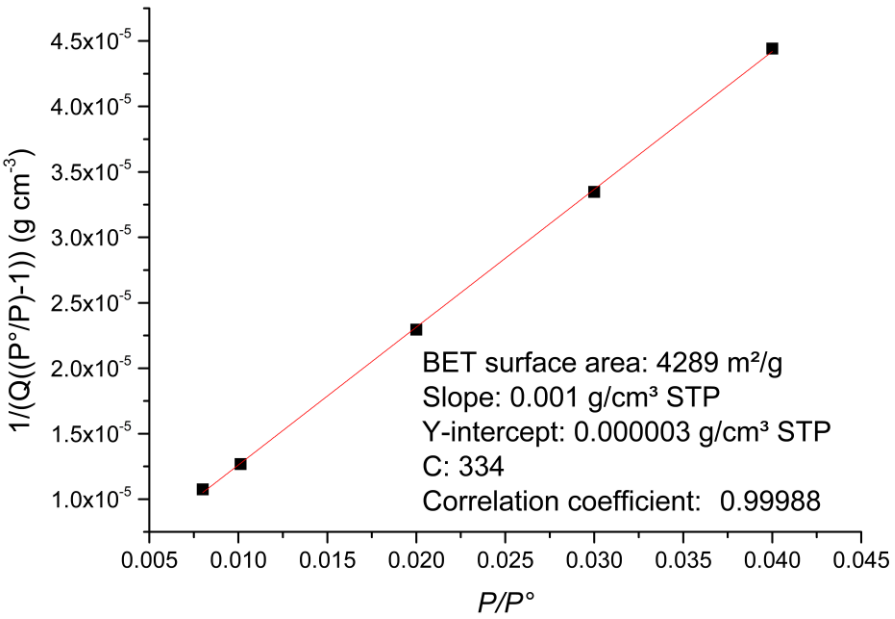

Figure S16. The BET plot derived from simulated N_2 uptake in MFM-184a.

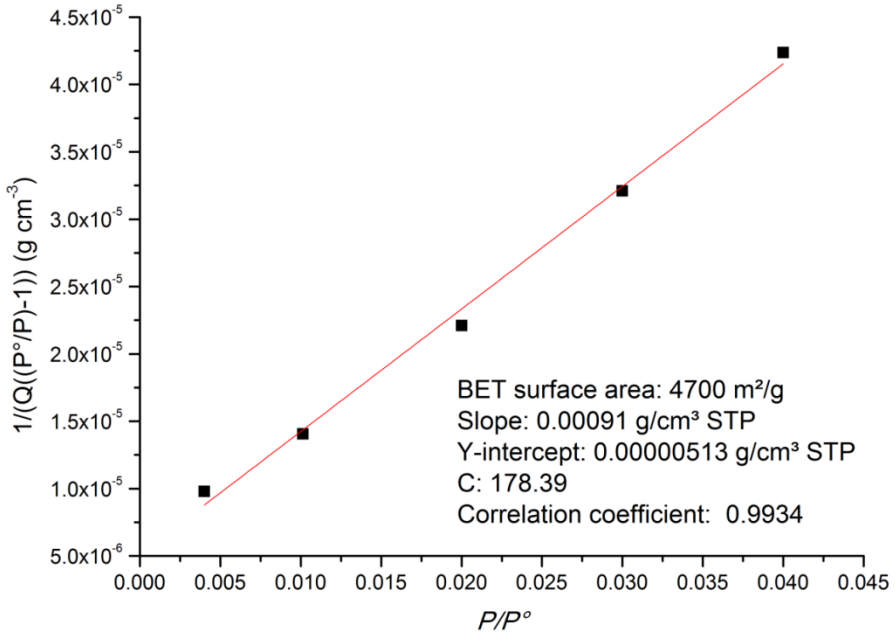

Figure S17. The BET plot derived from simulated N_2 uptake in MFM-185

Heats of adsorption for CO_2 and CH_4 in MFM-18X frameworks

The CO_2 and CH_4 adsorption isotherms at 273 and 298 K were fitted to the virial equation (eq 3, virial method I):[17]

$$\ln(n/P) = A_0 + A_1 * n + A_2 * n^2 + A_3 * n^3 + \ldots \quad (1)$$

where P is the pressure, n is total amount adsorbed and A_0, A_1, A_2, etc. are virial coefficients. The Henry's Law constant is given by $K_H = \exp(A_0)$. The enthalpy of adsorption at zero coverage was determined from the relationship:

$$\delta A_0 = R Q_{st}^{n=0} \delta(T^{-1}) \quad (2)$$

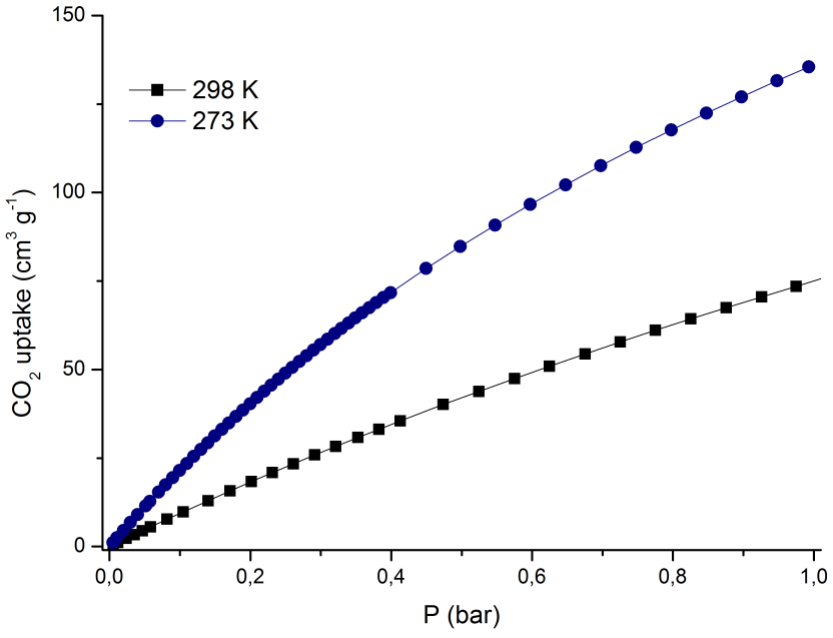

Figure S18. CO_2 sorption isotherms for MFM-180a at 273 and 298 K.

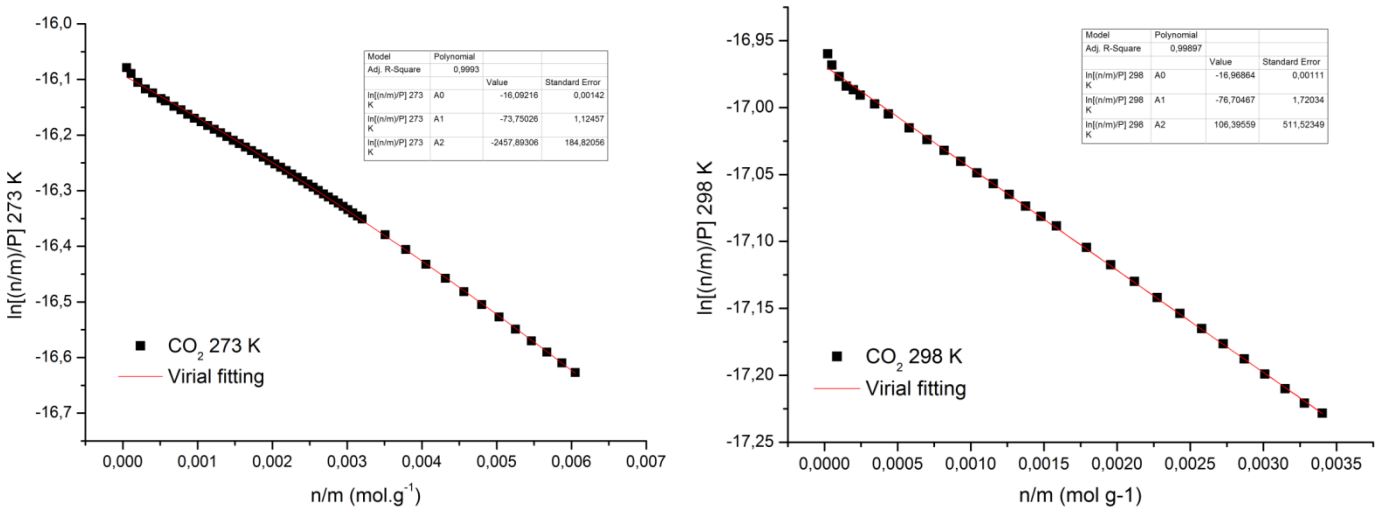

Figure S19. Virial analysis of the CO2 isotherms for MFM-180a at 298 and 273 K.

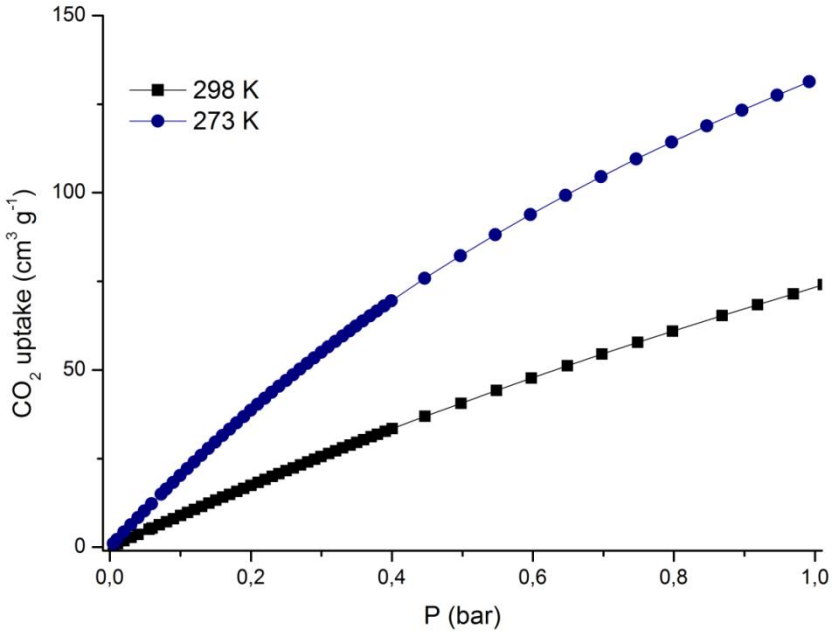

Figure S20. CO_2 sorption isotherms for MFM-181a at 273 and 298 K.

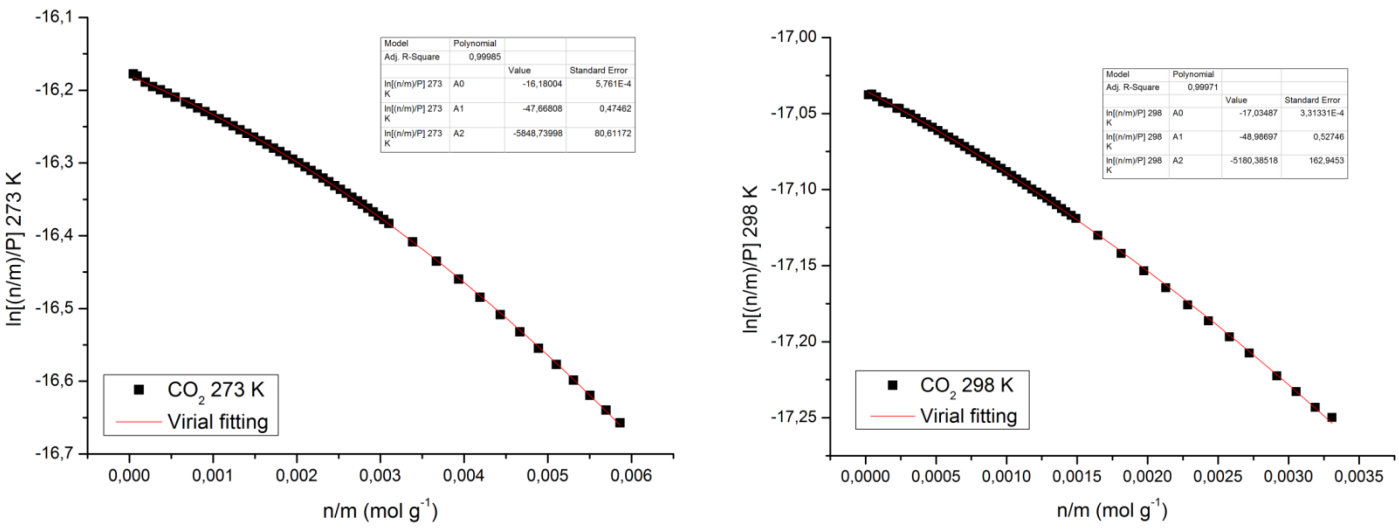

Figure S21. Virial analysis of the CO2 isotherms for MFM-181a at 298 and 273 K

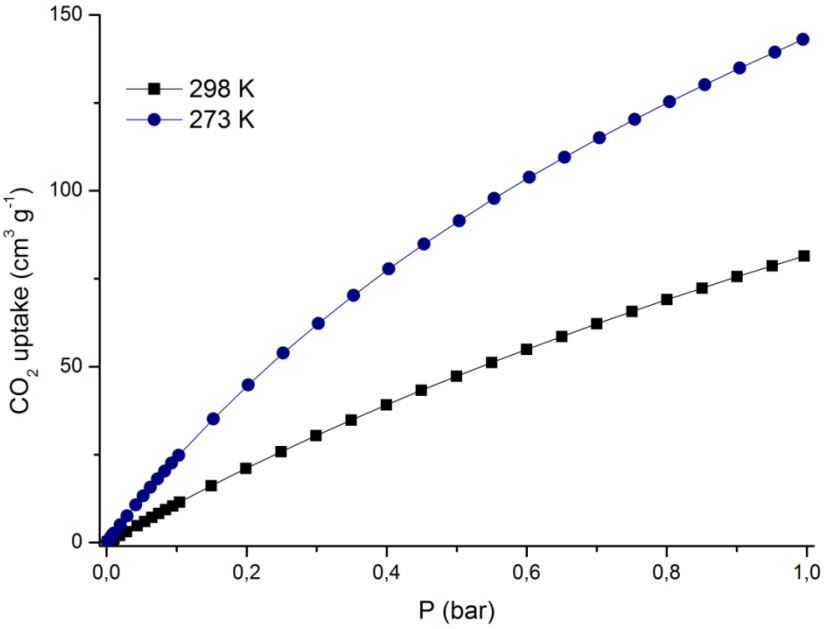

Figure S22. CO_2 sorption isotherms for MFM-183a at 273 and 298 K.

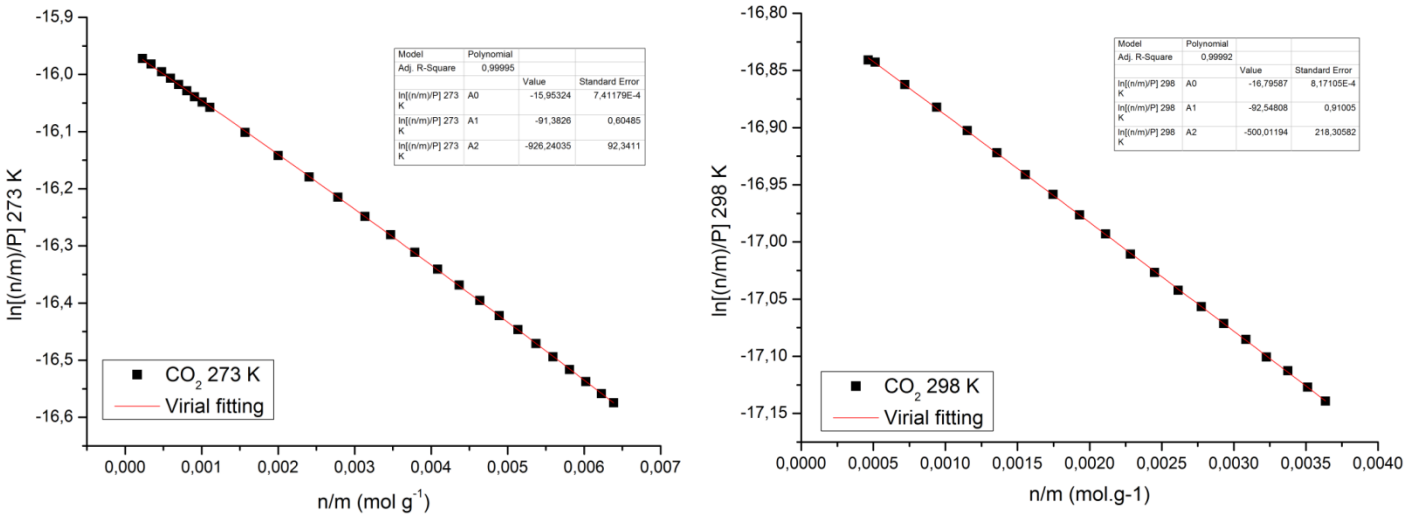

Figure S23. Virial analysis of the CO_2 isotherms for MFM-183a at 298 and 273 K

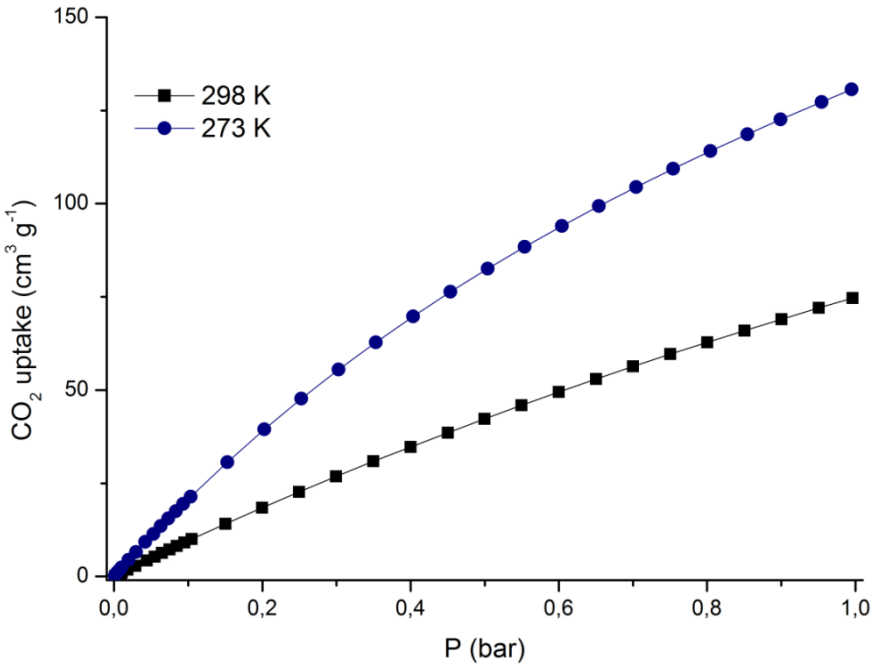

Figure S24. CO_2 sorption isotherms for MFM-185a at 273 and 298 K.

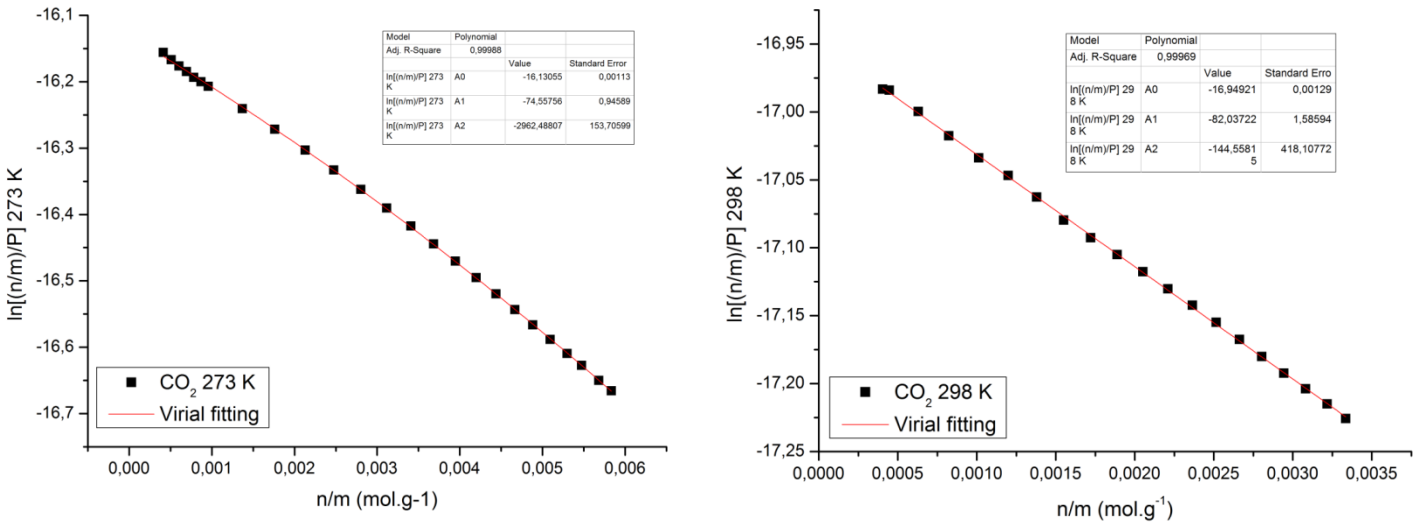

Figure S25. Virial analysis of the CO_2 isotherms for MFM-185a at 298 and 273 K

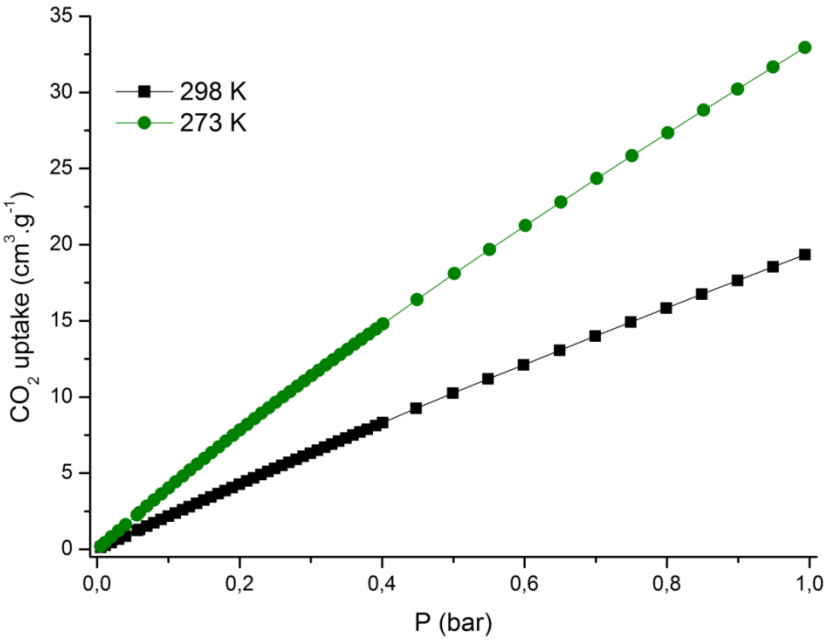

Figure S26. CH_4 sorption isotherms for MFM-180a at 273 and 298 K.

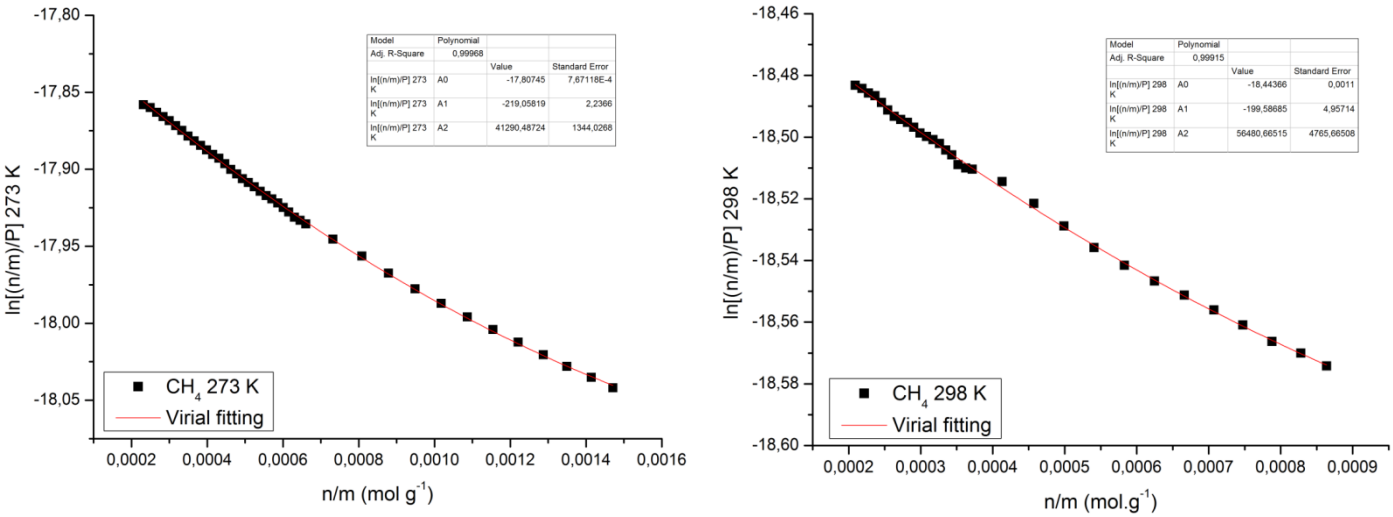

Figure S27. Virial analysis of the CH_4 isotherms for MFM-180a at 298 and 273 K

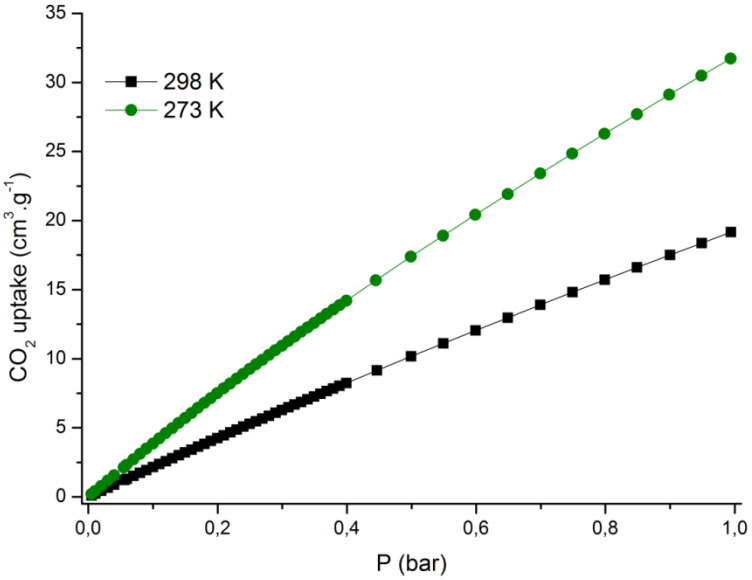

Figure S28. CH_4 sorption isotherms for MFM-181a at 273 and 298 K.

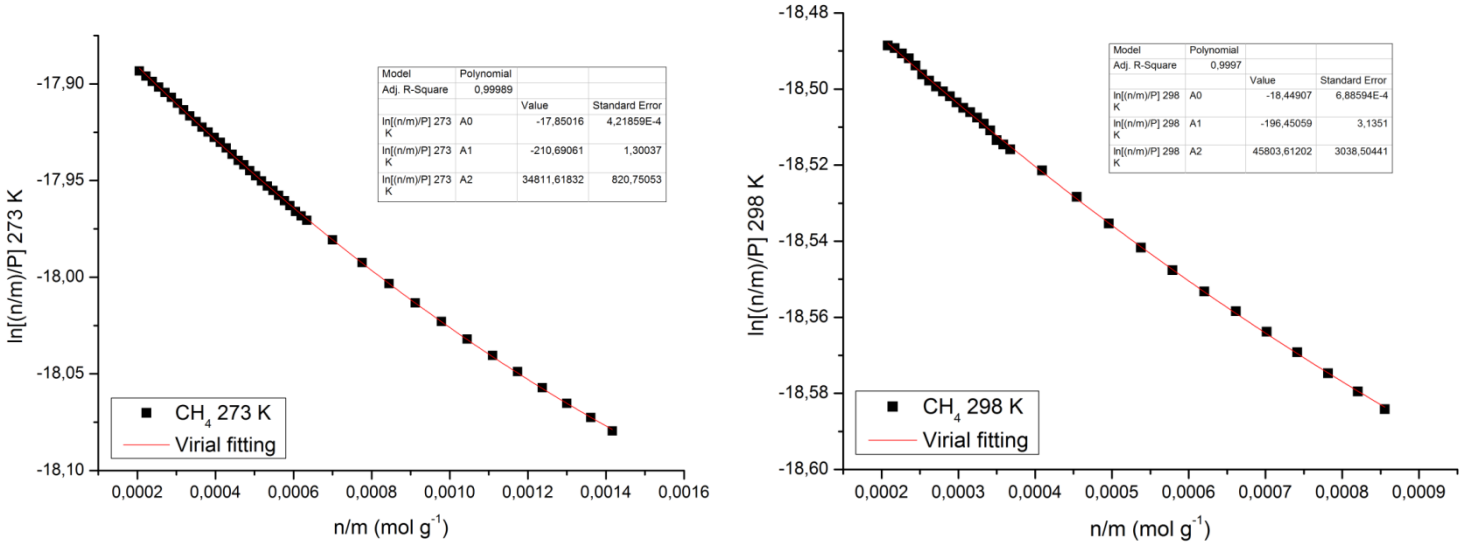

Figure S29. Virial analysis of the CH_4 isotherms for MFM-181a at 298 and 273 K

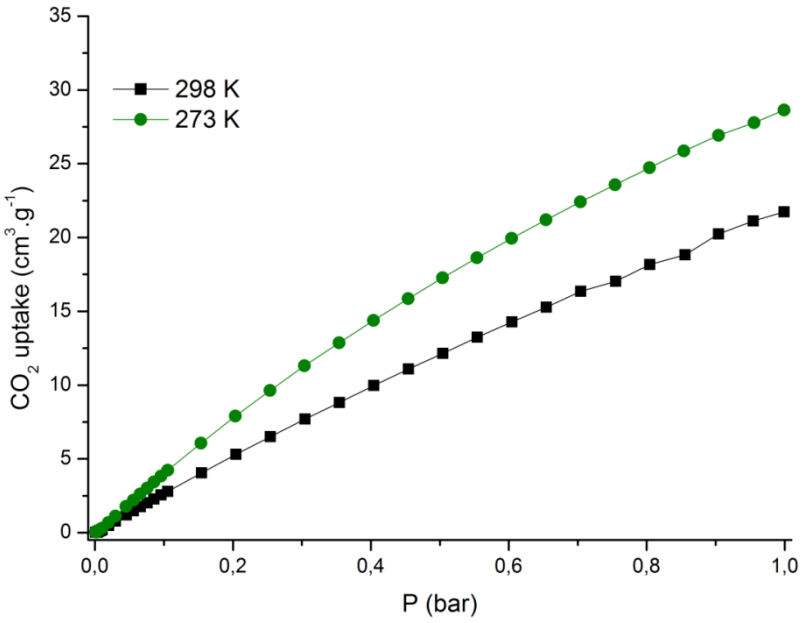

Figure S30. CH_4 sorption isotherms for MFM-183a at 273 and 298 K.

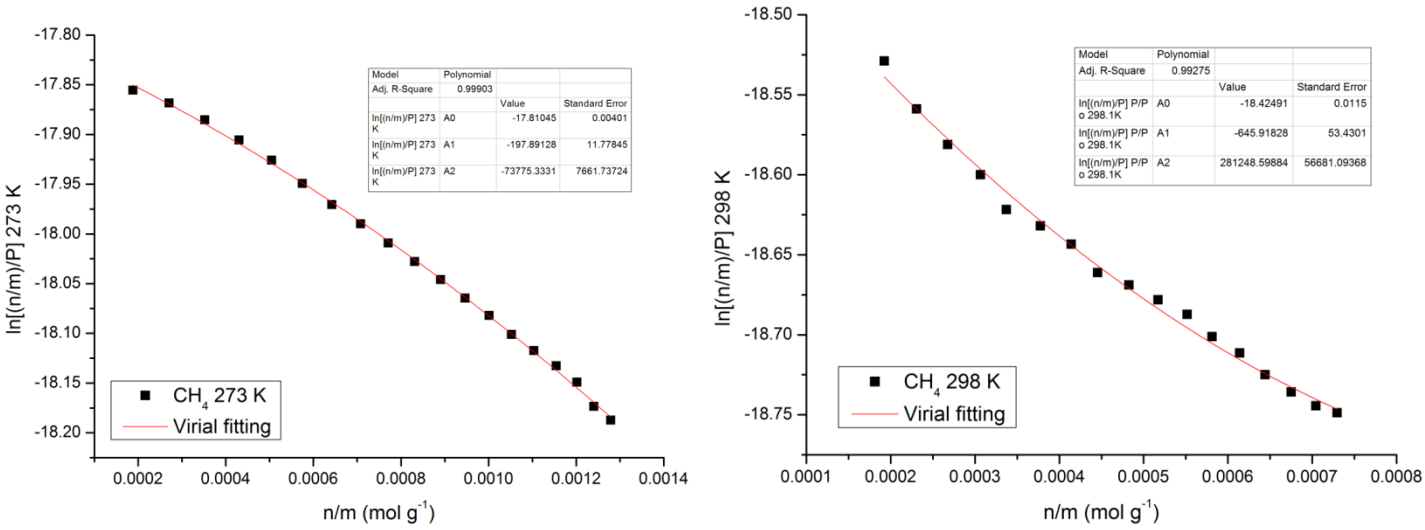

Figure S31. Virial analysis of the CH_4 isotherms for MFM-183a at 298 and 273 K

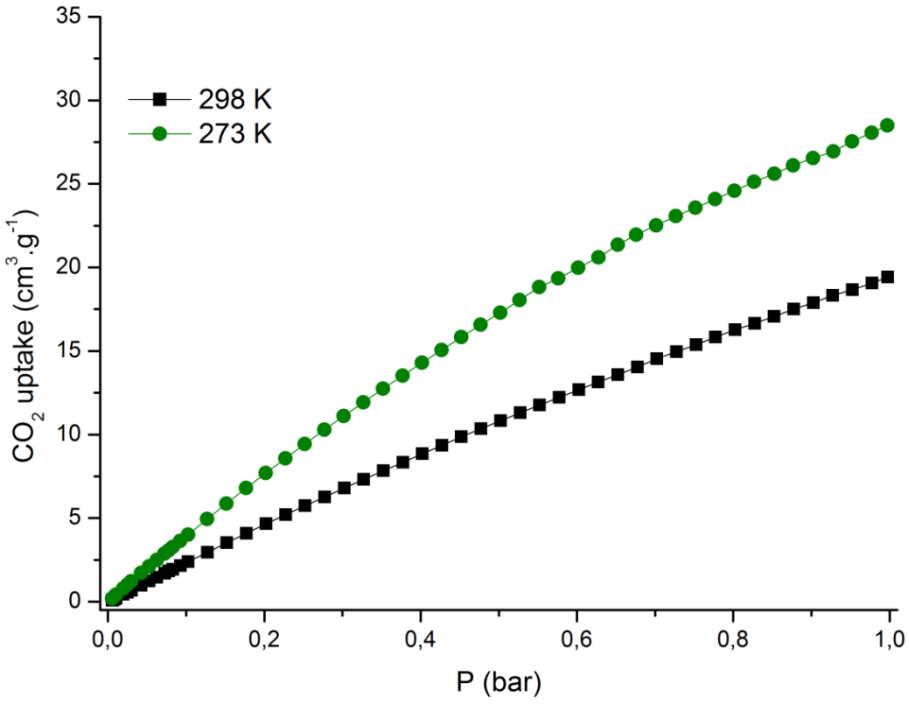

Figure S32. CH_4 sorption isotherms for MFM-185a at 273 and 298 K.

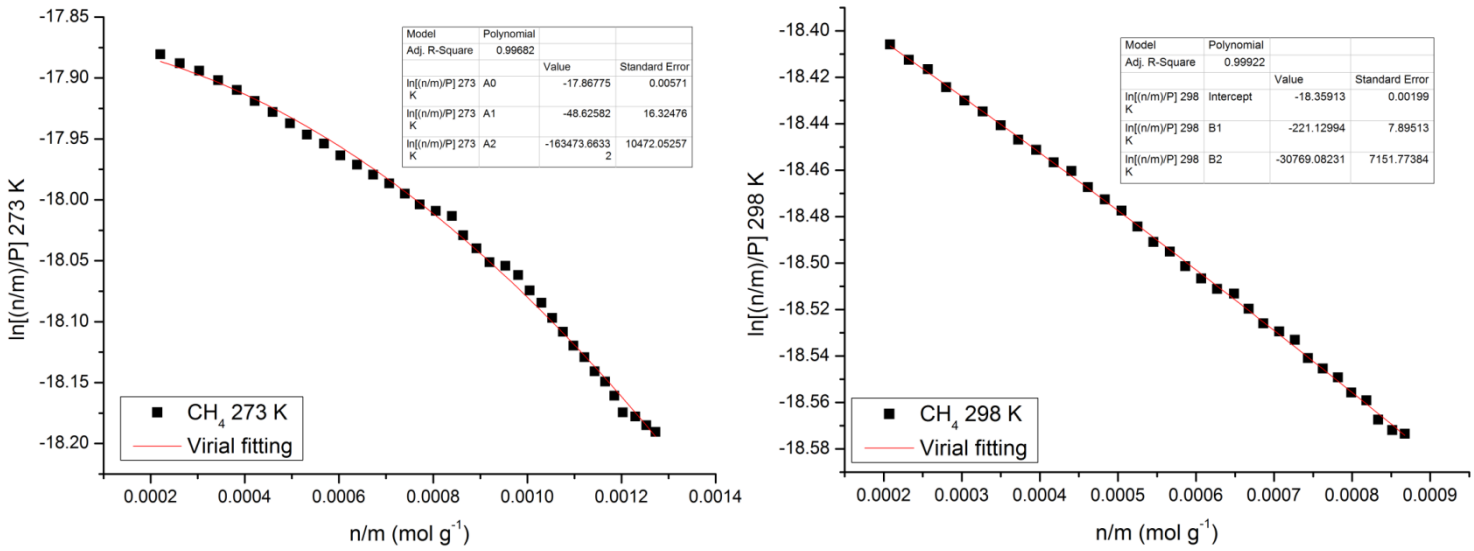

Figure S33. Virial analysis of the CH_4 isotherms for MFM-185a at 298 and 273 K

Table S6. Comparison of CH_4 adsorption properties for selected octacarboxylate $[Cu_2(O_2CR)_4]$ paddlewheel MOFs.

	CH_4 uptake [a] [g g^{-1}]	CH_4 uptake[a] [cm^3 cm^{-3} STP]	CH_4 uptake[b] [g g^{-1}]	CH_4 uptake[b] [cm^3 cm^{-3} STP]	Working capacity[c] [g g^{-1}]	Working capacity[c] [cm^3 cm^{-3}]	Q_{st} [kJmol^{-1}]
MFM-181	0.189	159	0.212	179	0.157	132	15.8
MFM-183	0.191	143	0.262	197	0.209	157	12.8
MFM-185	0.204	138	0.290	197	0.240	163	14.3
PCN-80[30]	0.177	142	-	-	-	-	-
Cu-tbo-MOF-5[31]	0.170	151	0.238	199	0.189	158	20.4

[a] 35 bar, 298 K; [b] 298 K, 65 bar; [c] 5-65 bar

Table S7. Comparison of CO_2 adsorption properties for selected octacarboxylate $[Cu_2(O_2CR)_4]$ paddlewheel MOFs.

	1 bar (298 K)		20 bar (298 K)		
	wt %	cm^3 cm^{-3} (STP)	wt %	cm^3 cm^{-3} (STP)	Q_{st} (kJ.mol^{-1})
MFM-180	15.0	49.8	83.1	276.5	23.7
MFM-181	14.6	44.6	95.4	292.4	23.1
MFM-183	13.7	37.2	96.7	263.3	22.9
MFM-185	13.0	32.2	107.3	265.0	22.7
PCN-80[30]	12.0	35.1	72.8	213.2	-
NOTT-140[23]	-	-	91.2[a]	314.2[a]	24.7

[a] 293 K

As reflected by their heat of adsorption of CO_2 and CH_4 at zero coverage, MFM-180a, 181a, 183a and 185a all show a selectivity for CO_2 compared to CH_4, consistent with these materials having open metal sites.[18] In general, CO_2 can interact with the MOF pore surface more strongly than CH_4 and N_2 due to its large quadrupole moment, leading to selective CO_2 uptakes. The CO_2/CH_4 selectivities calculated (initial slopes of the isotherms) for all MOFs in this series are distributed around 4 (MFM-180a: 4.41; MFM-181a: 4.12; MFM-183a: 3.95; MFM-185a: 4.09).

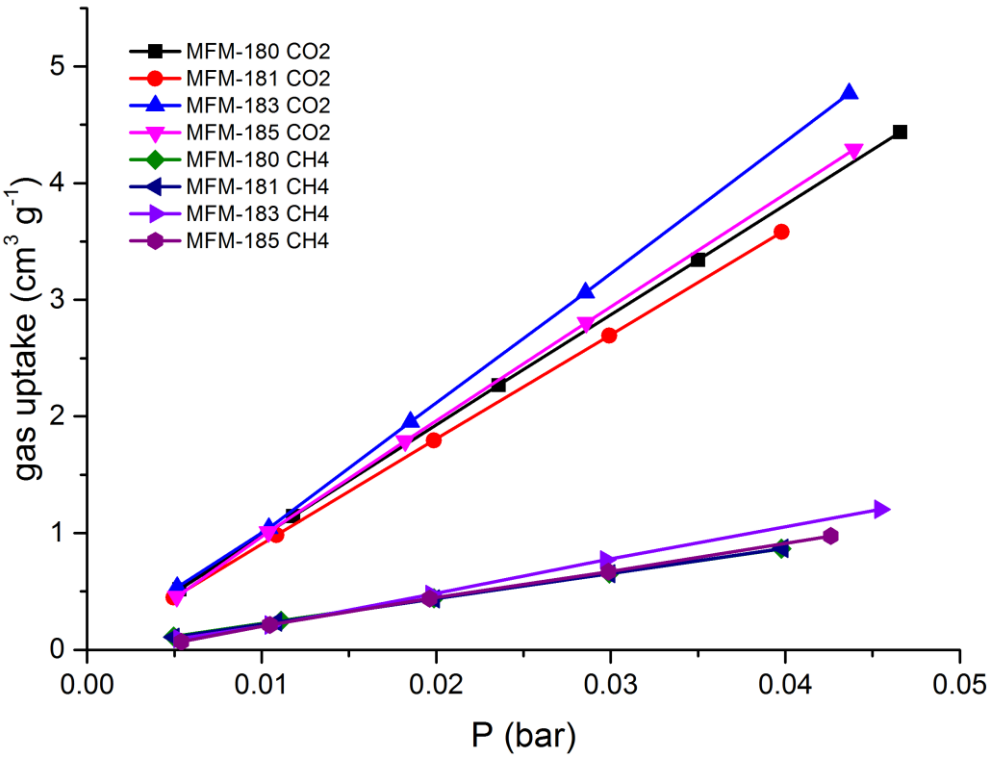

Figure S34. Comparison of the slopes of the low pressure, 298 K CO_2 and CH_4 adsorption isotherms.

Solid state ^{2}H NMR spectroscopy of deuterated MFM-180 and MFM-181 frameworks

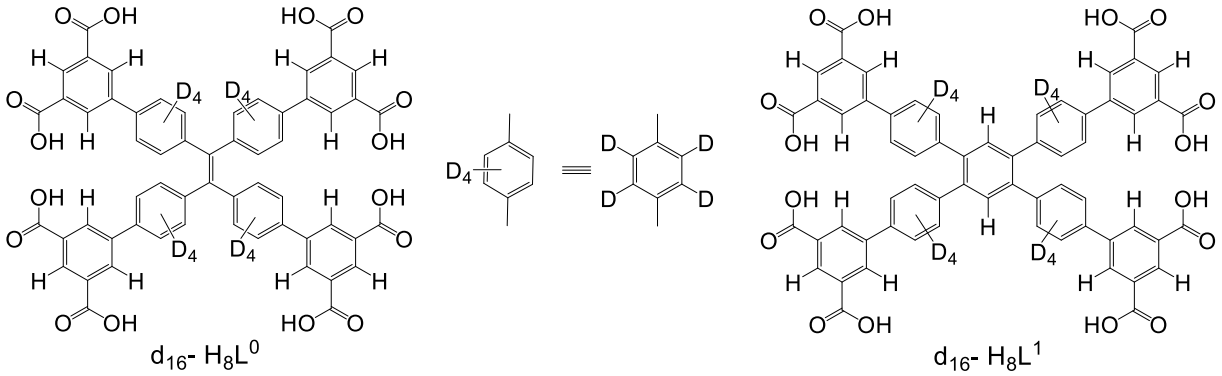

Scheme S2. The selectively deuterated linkers H_8L^0-d_{16} and H_8L^1-d_{16} used for the synthesis of deuterated MFM-180-d_{16} and MFM-181-d_{16}.

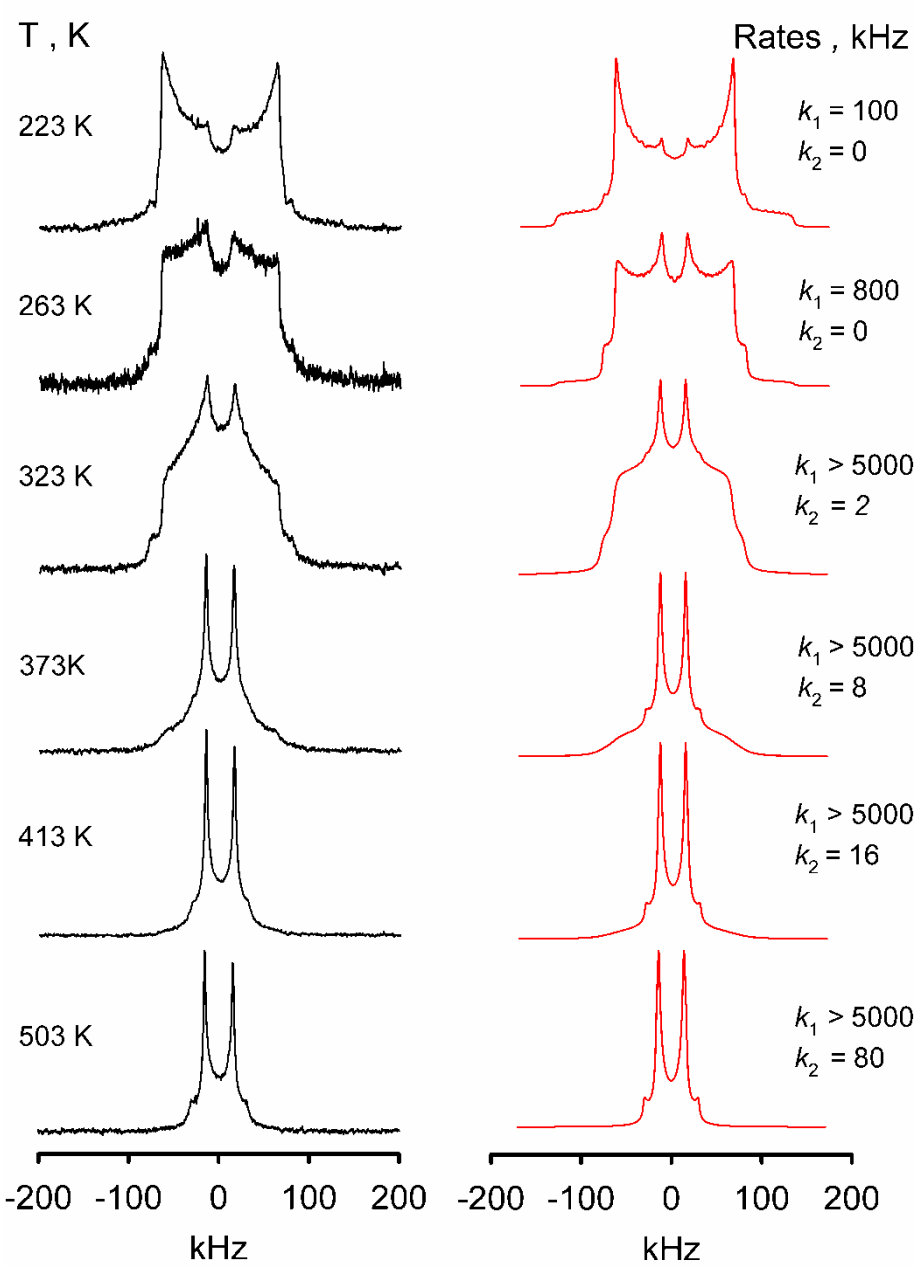

Figure S35. Temperature dependence of the ^{2}H NMR spectral line shape for the phenyl fragments in MFM-180-d_{16} (experimental - black, simulation - red). 2-Site exchange patterns were observed for T < 323 K requiring the introduction of a distribution of flipping rate constants; we assumed a log-normal distribution with a distribution width **σ** ~ 1. The line-width was taken to be **dω** = 0.5 kHz.

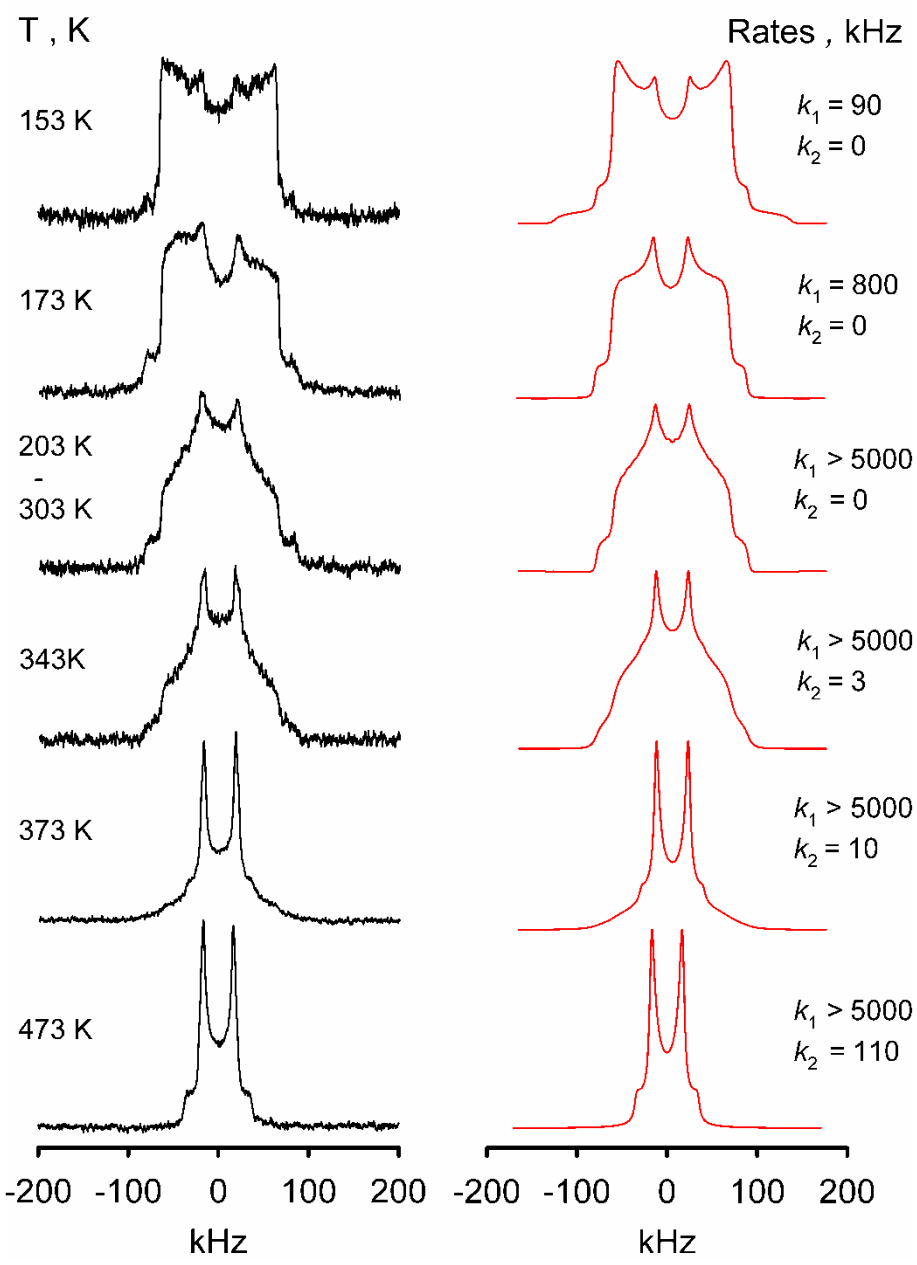

Figure S36. Temperature dependence of the ^{2}H NMR spectral line shape for the phenyl fragments in MFM-181-d_{16} (experimental - black, simulation - red). 2-Site exchange patterns were observed for T < 343 K requiring the introduction of a distribution of flipping rate constants; we assumed a log-normal distribution with a distribution width **σ** ~ 2. The line-width was taken to be **dω** = 2 kHz.

^{2}H NMR spectra line shape simulation.

To understand the detailed mechanism of rotations and their kinetic parameters (the activations barriers and rate constants), a detailed fitting analysis of the ^{2}H NMR spectral line shape across a temperature range was performed. The FORTRAN simulation routines used are based on the general formalism proposed by Abragam[19] and developed in detail by Spiess[20] and others.[21–24] The fitted spectra were obtained by Fourier transform of the powder-average over the polar angles θ and φ of the correlation function $G(t,\theta,\varphi)$, which governs the time evolution of the transverse ^{2}H spin magnetization after the solid echo pulse sequence. The correlation function can be computed using the following equation:[22]

$$G(t,\theta,\varphi) = \sum_{i,j,k}^{1..N} \mathbf{l}_i \left[\exp(\mathbf{A}t)\right]_{ij} \left[\exp(\mathbf{A}\tau)\right]_{ij} \left[\exp(\mathbf{A}*\tau)\right]_{jk} \mathbf{P}_k \,, \tag{1}$$

where **A** is a complex matrix composed as follows:

$$\mathbf{A} = \Omega + \mathrm{K}\,, \tag{2}$$

The diagonal matrix Ω is composed by elements ω_i describing the frequencies of the exchanging sites, and K corresponds to a kinetic matrix that defines the jump rates.

$$\begin{cases} \Omega_{ii} = i\omega_i - 1/T_2{}^0 \\ \Omega_{ij} = 0 \end{cases} \quad \text{and} \quad \begin{cases} \mathrm{K}_{ii} = -\sum_{j\neq i} k_{ij} \\ \mathrm{K}_{ij} = k_{ij} \end{cases}, \tag{3}$$

The $1/T_2{}^0$ term is the residual line width which reflects the contributions from homo- and heteronuclear dipolar interactions of the spin Hamiltonian. **l** is a vector (1,1,…,1) with N elements, where N is the number of exchange sites. **P** is a vector of equilibrium population of each site $p_{eq}(i)$. k_{ij} is the exchange rate between sites i and j. The ^{2}H NMR frequency at the i-th site $\omega_i(\theta,\varphi)$ is defined as:

$$\begin{aligned} \omega_i(\theta,\varphi) &= \sqrt{\frac{3}{2}}\frac{1}{2}\sum_{a,b=-2}^{2} q_{2a} D_{ba}(\Omega^i) D_{a0}(\varphi,\theta,0) \\ q_2 &= \left(-\frac{\eta}{2}, 0, \sqrt{\frac{3}{2}}, 0, -\frac{\eta}{2}\right) Q \end{aligned} \tag{4}$$

Here $D_{ba}(\Omega)$ are the Wigner rotation matrices[20] defining the C-D bond orientation for each site and q_2 is the static quadrupolar coupling tensor, with the Wigner matrices as defined by Spiess.[20] The q_2

tensor of a given deuteron is defined in the principle axis system (PAS), *i.e.*, a frame with the Z axis aligned with regard to C-D bond orientation. If the motion is complex, then the Winger matrix responsible for the transformation of the C-D bond orientation from the PAS (n = 1) frame to the frame attached to the molecular axis system (or the crystalline axis system, n=N) is a result of action of multiple Wigner matrices, each responsible for a certain rotation, *i.e.*,

$$D_{ba}(\Omega^{i}) = \sum_{c,d=-2}^{2} D_{bc}(\Omega^{1}) D_{cd}(\Omega^{\cdots}) D_{da}(\Omega^{N}) \tag{5}$$

In other words, to apply such jump-model concept to the particular case of the dynamics of the phenyl ring, a certain mechanism for these rotations has to be specified: a set of rotational matrices and the rate matrix that defines the exchange mechanism. Below is a typical and illustrative example of a 180° 2-site exchange case:

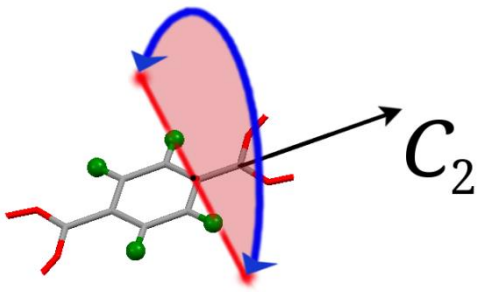

Figure S37: A phenyl ring exhibiting a large-amplitude 180° flips around the C_2 symmetry axis.

The 180° flips about the C_2 axis can be described by a 2x2 rate exchange matrix K:

$$K = \begin{bmatrix} -k_1 & k_1 \\ k_1 & -k_1 \end{bmatrix} \tag{6}$$

In the case when one of the motional process is characterized by a broad distribution of correlation times, the simulation procedure must be modified to take this into account. Physical reasons for such distribution are associated with samples inhomogeneity, either present due to the defects of the crystal structure, either induced by guests or other physical stimuli.

In our case, the flipping rate $k_f = k_1$ is characterized by a distribution. Since this distribution is broad and almost static over a broad temperature region, it can be assumed that the physical reason behind this is the variation in the torsional potential from one site to another. These variations are assumed to be randomly distributed and stable within the material sample. Such assumptions bring us to the log-normal distribution for the flipping rates constant k_f:

$$P(\ln k_f) = \frac{\exp[-\ln^2 k_f / k_{fm}]}{(2\pi)^{1/2}\sigma_E} \tag{7}$$

Then to the sum the weighted spectra we write:

$$G(t) = \int_{-\infty}^{\infty} g(t, k_f) P(\ln k_f) d \ln k_f \tag{8}$$

where $g(t, k_f)$ is the individual simulated FID.

Passing to a discrete distribution we get:

$$G(t) = \sum_{i=1..N} g(t, k_f{}^i) W^i \tag{9}$$

Where the individual weights are computed as:

$$W^i = \frac{\int_{\ln k_f{}^i}^{\ln k_f{}^{i+1}} P(\ln k) d \ln k}{Norm} \tag{10}$$

The Norm is calculated as:

$$Norm = \sum_{i=1..N} W^i \tag{11}$$

Such modification to the original fitting routine allows us to take into account the rate exchange distribution for any motion(s). Within such an approach any rate constant will be characterized by 2 parameters: σ - the width of the distribution, and k_{fm} – the mean value of the rate constant, *i.e.*, the center of the distribution. The k_{fm} temperature behavior should characterize the mean Arrhenius parameters of the motion in the sample, *i.e.*, the activation barrier and collision factor. So, on a descriptive level, the sample at each temperature will be characterized by 3 population factors for: (a) static on the ^{2}H NMR time-scale phenyl rings ($k_f < 10^3$ Hz << Q_0; $Q_0 = 176 \cdot 10^3$ Hz), (b) slowly mobile phenyls (10^3 Hz < k_f < 10^7 Hz) and (c) fast moving fragments ($k_f > 10^7$ Hz >> Q_0).

(1) Noguchi, H.; Hojo, K.; Suginome, M. *J. Am. Chem. Soc.* **2007**, *129*, 758.

(2) Vyas, V. S.; Banerjee, M.; Rathore, R.; *Tetrahedron Lett.* **2009**, *50*, 6159.

(3) Lin, X.; Telepeni, I.; Blake, A. J.; Dailly, A.; Brown, C. M.; Simmons, J. M.; Zoppi, M.; Walker, G. S.; Thomas, K. M.; Mays, T. J.; Hubberstey, P.; Champness, N. R.; Schröder, M. *J. Am. Chem. Soc.* **2009**, *131*, 2159.

(4) Rodríguez-Lojo, D.; Cobas, A.; Peña, D.; Pérez, D.; Guitián, E. *Org. Lett.* **2012**, *14*, 1363.

(5) Chichak, K.; Jacquemard, U.; Branda, N. R. *Eur. J. Inorg. Chem.* **2002**, *2002*, 357.

(6) Shustova, N. B.; Ong, T.-C.; Cozzolino, A. F.; Michaelis, V. K.; Griffin, R. G.; Dincă, M. *J. Am. Chem. Soc.* **2012**, *134*, 15061.

(7) Sheldrick, G. M. *Acta Crystallogr. A* **2008**, *64*, 112.

(8) Sheldrick, G. M. *Acta Crystallogr. Sect. C Struct. Chem.* **2015**, *71*, 3.

(9) Spek, A. L. *Acta Crystallogr. Sect. C Struct. Chem.* **2015**, *71*, 9.

(10) Rouquerol, J.; Llewellyn, P.; Rouquerol, F. In *Studies in Surface Science and Catalysis*; 2007; Vol. 160, pp 49–56.

(11) Rappe, A. K.; Casewit, C. J.; Colwell, K. S.; Goddard, W. A.; Skiff, W. M. *J. Am. Chem. Soc.* **1992**, *114*, 10024

(12) Gupta, A.; Chempath, S.; Sanborn, M. J.; Clark, L. A.; Snurr, R. Q. *Mol. Simul.* **2003**, *29*, 29.

(13) Jorgensen, W. L.; Laird, E. R.; Nguyen, T. B.; Tirado-Rives, J. *J. Comput. Chem.* **1993**, *14*, 206.

(14) Rappé, A. K.; Casewit, C. J.; Colwell, K. S.; Goddard Iii, W. A.; Skiff, W. M. *J. Am. Chem. Soc.* **1992**, *114*, 10024.

(15) Potoff, J. J.; Siepmann, J. I. *AIChE J.* **2001**, *47*, 1676.

(16) Walton, K. S.; Snurr, R. Q. *J. Am. Chem. Soc.* **2007**, *129*, 8552.

(17) O'koye, I. P.; Benham, M.; Thomas, K. M. *Langmuir* **1997**, *13*, 4054.

(18) Wang, Q. M.; Shen, D.; Bülow, M; Lau, M. L.; Deng, S.; Fitch, F. R.; Lemcoff, L. O.; Semanscin, J. *Micropor. Mesopor. Mat.* **2002**, *55*, 217.

(19) Abragam, A. *The Principles of Nuclear Magnetism*; Oxford University Press, 1961.

(20) H. W. Spiess. Springer-Verlag, 1978; Vol. 15, p 55.

(21) Wittebort, R. J.; Szabo, A. *J. Chem. Phys.* **1978**, *69*, 1722.

(22) Wittebort, R. J.; Olejniczak, E. T.; Griffin, R. G. *J. Chem. Phys.* **1987**, *86*, 5411.

(23) Lipari, G.; Szabo, A. *Biophys. J.* **1980**, *30*, 489.

(24) Schwartz, L. J.; Meirovitch, E.; Ripmeester, J. A.; Freed, J. H. *J. Phys. Chem.* **1983**, *87*, 4453.